

Kondo effects in a triangular triple quantum dot: NRG study in the whole region of the electron filling

Takahide Numata¹, Yunori Nisikawa¹, Akira Oguri¹, and Alex C. Hewson²

¹ Graduate School of Science, Osaka City University, Osaka 558-8585, Japan and

² Department of Mathematics, Imperial College, 180 Queen's Gate, London SW7 2BZ, UK

(Dated: November 9, 2018)

We study the low-energy properties of a triangular triple quantum dot connected to two non-interacting leads in a wide parameter range, using the numerical renormalization group (NRG). Various kinds of Kondo effects take place in this system depending on the electron filling N_{tot} , or the level position ϵ_d of the triple dot. The SU(4) Kondo behavior is seen in the half-filled case $N_{\text{tot}} \simeq 3.0$ at the dip of the series conductance, and it causes a charge redistribution between the even and odd orbitals in the triangle. We show generally that the quasi-particle excitations from a local Fermi-liquid ground state acquire a channel symmetry at zero points of the two-terminal conductance, in the case the system has time-reversal and inversion symmetries. It causes the SU(4) behavior at low energies, while the orbital degeneracy in the triangle determines the high-energy behavior. At four-electron filling $N_{\text{tot}} \simeq 4.0$, a local $S = 1$ moment emerges at high temperatures due to a Nagaoka ferromagnetic mechanism. It is fully screened by the electrons from the two conducting channels via a two-stage Kondo effect, which is caused by a difference in the charge distribution in the even and odd orbitals.

PACS numbers: 72.10.-d, 72.10.Bg, 73.40.-c

I. INTRODUCTION

The Kondo effect in quantum dots is an active field of current research.^{1,2,3,4} It has been studied in various situations, such as Aharonov-Bohm (AB) rings,^{5,6,7,8} tunneling junctions coupled to superconducting hosts,^{9,10,11,12,13,14,15} and a number of multi-dot and multi-orbital systems.^{16,17,18,19} Due to the variety of combinations of quantum dots that can be fabricated, and their high tunability, it is possible to study novel interplays between the strong electron correlation and quantum-mechanical interference effects. These were once studied as different topics in the field of the condensed matter physics.

The triangular triple quantum dot (TTQD) is an interesting system, which can demonstrate various types of the Kondo effects depending on an external field, the electron filling N_{tot} , and so on.^{20,21} For instance, a closed path along the triangle under a magnetic field can work as an AB interferometer.²⁰ Also in the case four electrons occupying the cluster of the triple dot, $N_{\text{tot}} = 4.0$, the closed loop induces a local $S = 1$ moment due to a Nagaoka ferromagnetic mechanism.²¹ Furthermore, the orbital degrees of freedom cause a sharp conductance dip appearing at half-filling $N_{\text{tot}} = 3.0$,²¹ which links to the SU(4) Kondo effects. These features distinguish the TTQD from a linear chain of three quantum dots,^{22,23,24,25,26,27} and from the other three-level systems.^{28,29,30,31,32,33} Experimentally, triple quantum-dot systems have been realized in AlGaAs/GaAs heterostructure,^{34,35,36} self-assembled InAs,³⁷ and a single wall carbon nanotube.³⁸ The triangular trimmer of Cr atoms placed upon an Au surface is also a related system.^{39,40,41}

The TTQD has a big parameter space to be explored,

and the number of the conducting channels which are coupled to the triangle also gives interesting variations in low-energy properties.^{42,43,44,45} In Refs. 43 and 44 the TTQD's connected, respectively, to two leads⁴³ and one lead⁴⁴ were studied. The main interest in these two recent works was the behavior at half-filling $N_{\text{tot}} \simeq 3.0$, but the effects of the gate voltage ϵ_d which varies the electron filling in the TTQD were not examined. The other recent report Ref. 45 addresses the effects of ϵ_d in the cases of the two and three leads, but the parameter region examined was restricted in a small interaction U and a large dot-lead coupling Γ . In the previous works we studied the TTQD connected to two leads,^{21,42} and showed that the various types of the Kondo behavior clearly take place at different values of the gate voltage. The calculations were carried out, however, for a typical but just one parameter set which describes a large U and small Γ situation.

The purpose of the present work is to study the feature of the Kondo behavior in the TTQD connected to two leads in a wide parameter range. To this end, we calculate the conductance and scattering phase shifts at zero temperature, making use of the numerical renormalization group (NRG). Furthermore, we calculate also the TTQD contributions to the entropy and spin susceptibility, and from their temperature dependence we deduce the Kondo energy scale. Our results reveal the precise features of the Kondo behavior in a wide parameter region of the electron filling N_{tot} , interaction U , and the hybridization energy scale Γ . For instance, the $S = 1$ moment is fully screened at low temperatures via two separate stages by the conduction electrons from the two non-interacting leads, which break the C_{3v} symmetry of the triangle. The two-stage screening process reflects the charge distribution in the even and odd orbitals which are classified according to the parity. It is confirmed

that the $S = 1$ Kondo behavior can be seen in a wide parameter region for $N_{\text{tot}} = 4.0$. It is robust against the perturbations the typical energy of which is less than the finite energy separation between the Nagaoka and the first excited states for the triangular cluster. Specifically, the $S = 1$ Kondo behavior is not sensitive to the deformations of the TTQD caused by the inhomogeneities in the level positions and the inter-dot hopping matrix elements.

We show also that the fixed-point Hamiltonian, which describes the low-lying quasi-particle excitations from a local Fermi-liquid ground state, acquires an $SU(2)$ symmetry between the even and odd channels at zero points of the two-terminal conductance, in the case that the system has time-reversal and inversion symmetries. It means that if the phase shifts for the even and odd channels satisfy the condition $\delta_e - \delta_o = n\pi$ for $n = 0, \pm 1, \pm 2, \dots$, then the low-energy behavior can be characterized by an $SU(4)$ symmetric Fermi-liquid theory with the channel and spin symmetries, even if the original Hamiltonian does not have the $SU(4)$ symmetry on a global energy scale. This happens quite generally for multi-dot and multi-orbital systems. In the case of the TTQD connected to two conducting channels, there are three zero points at most. Particularly, the one at half-filling $N_{\text{tot}} = 3.0$ shows a pronounced behavior as a sharp dip in the Kondo plateau.^{21,42} At this zero point the system has an $SU(4)$ symmetry not only at low energies but also at high energies, which is caused by the orbital degeneracy in the cluster of the regular triangular. These symmetric properties cause the $SU(4)$ Kondo behavior^{46,47,48,49} seen in a wide temperature range.⁴² Away from this zero point at the dip the NRG results of the thermodynamic quantities show that the channel symmetry is broken at low temperatures, and we observe the $SU(2)$ Kondo behavior due to the spin. We find also that the sharp dip structure of the series conductance does not disappear from the Kondo plateau, even in the presence of infinitesimal deformations which break the C_{3v} symmetry, although the position of the dip shifts from the middle of the plateau as the deformation increases.

We study also the characteristic temperature T^* , at which a crossover to a singlet ground state take place, for a wide range of the electron filling N_{tot} . The result shows that T^* becomes high at the conductance dip for $N_{\text{tot}} = 3.0$ due to the $SU(4)$ Kondo behavior. It is enhanced also at a mixed-valence point, where the ground-state energy for $N_{\text{tot}} = 3.0$ and that for $N_{\text{tot}} = 4.0$ coincide. Furthermore, the screening temperature T^* increases as the hybridization energy scale Γ increases, which would raise the experimental accessibility to the low-temperature Fermi-liquid region.

The paper is organized as follows. In Sec. II, we give the outline a description of the model and the formulation. In Sec. III, we describe the low-energy channel symmetry that the fixed-point Hamiltonian acquire at the zero point of the two-terminal conductance. The NRG

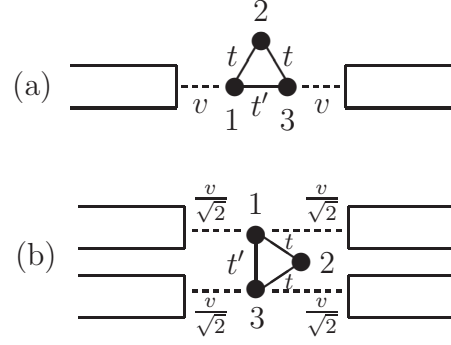


FIG. 1: Triangular triple quantum dot in (a) series and (b) parallel configurations. The dot labelled with $i = 2$ is referred to as the *apex* site, which has no direct connection to the leads.

results for the ground-state properties are presented in Sec. IV. The results for temperature dependence of the TTQD contributions of entropy and spin susceptibility are presented in Sec. V. The effects of the deformations which breaks the triangular symmetry are discussed in Sec. VI. A summary is given in Sec. VII.

II. FORMULATION

In this section we describe the model and the formulation which we have employed in the present work. We also describe some particular characteristics of the triangular triple dot in the two solvable limits, $\Gamma = 0$ and $U = 0$, in order to see the essential ingredients that cause the various Kondo effects taking place in this system.

A. Model

We start with a three-site Hubbard model on a triangle that is connected to two non-interacting leads on the left (L) and right (R), at the sites labelled by $i = 1$ and $i = N_D (\equiv 3)$, respectively, as illustrated in Fig. 1 (a). The Hamiltonian is given by

$$\mathcal{H} = \mathcal{H}_{\text{dot}}^0 + \mathcal{H}_{\text{dot}}^U + \mathcal{H}_{\text{mix}} + \mathcal{H}_{\text{lead}}, \quad (1)$$

$$\begin{aligned} \mathcal{H}_{\text{dot}}^0 = & - \sum_{\langle ij \rangle} \sum_{\sigma} t_{ij} \left(d_{i\sigma}^{\dagger} d_{j\sigma} + d_{j\sigma}^{\dagger} d_{i\sigma} \right) \\ & + \sum_{i=1}^{N_D} \sum_{\sigma} \epsilon_{d,i} d_{i\sigma}^{\dagger} d_{i\sigma}, \end{aligned} \quad (2)$$

$$\mathcal{H}_{\text{dot}}^U = U \sum_{i=1}^{N_D} n_{d,i\uparrow} n_{d,i\downarrow}, \quad n_{d,i\sigma} \equiv d_{i\sigma}^{\dagger} d_{i\sigma}, \quad (3)$$

$$\mathcal{H}_{\text{mix}} = \sum_{\sigma} \left(v_L d_{1,\sigma}^{\dagger} C_{L\sigma} + v_R d_{N_D,\sigma}^{\dagger} C_{R\sigma} + \text{H.c.} \right), \quad (4)$$

$$\mathcal{H}_{\text{lead}} = \sum_{\nu=L,R} \sum_{k\sigma} \epsilon_k c_{k\nu\sigma}^{\dagger} c_{k\nu\sigma}. \quad (5)$$

Here, $d_{i\sigma}^\dagger$ creates an electron with spin σ at the i -th site in the dot, $\epsilon_{d,i}$ the onsite energy in the dot, and U the Coulomb interaction. The hopping matrix elements t_{ij} between the dots are chosen to be positive ($t_{ij} > 0$). The conduction electrons near the dots, $C_{\nu\sigma} \equiv \sum_k c_{k\nu\sigma}/\sqrt{N}$, can tunnel into the triangle via the hybridization term Eq. (4), which causes the level broadening $\Gamma_\nu \equiv \pi\rho v_\nu^2$, with ρ the density of states of the leads. In the present work we consider the equal-coupling case $\Gamma_L = \Gamma_R (\equiv \Gamma)$, namely $v_L = v_R (\equiv v)$, and assume that the system has an inversion symmetry taking $\epsilon_{d,1} = \epsilon_{d,3} (\equiv \epsilon_d)$, $t_{12} = t_{23} (\equiv t)$ and $t_{13} (\equiv t')$. We shall refer to the dot at $i = 2$ in Fig. 1 as the *apex* site $\epsilon_{d,2} \equiv \epsilon_{\text{apex}}$, and choose the Fermi energy E_F as the origin of the energy $E_F = 0$.

B. Cluster of the triangular triple dot

In order to see some characteristic features of the system, we first of all discuss a cluster of a triangular triple dot, described by $\mathcal{H}_{\text{dot}}^0 + \mathcal{H}_{\text{dot}}^U$. The eigenstates and energies of this cluster give us a clue to understand the high-energy properties of the system. To be specific, we consider a regular triangle case, choosing $\epsilon_{\text{apex}} = \epsilon_d$ and $t' = t$.

In the non-interacting case the one-particle states of $\mathcal{H}_{\text{dot}}^0$ can be labelled by a wavenumber k ($= 0, \pm 2\pi/3$), and the eigenvalues are given by $E_k^{(1)} = -2t \cos k + \epsilon_d$,

$$E_{k=0}^{(1)} = -2t + \epsilon_d, \quad E_{k=\pm \frac{2\pi}{3}}^{(1)} = t + \epsilon_d. \quad (6)$$

The excited states, for $t > 0$, are degenerate with respect to $k = \pm 2\pi/3$. This degeneracy brings interesting varieties to the Kondo effects depending on the occupation number N_{tot} , or ϵ_d , which can be controlled by the gate voltage. In the case that the number of electrons is $N_{\text{tot}} = 3$, namely at half-filling, the ground state for the triangular cluster has the four-fold degeneracy due to the orbital and spin degrees of freedoms. This is because the first two electrons occupy the one-particle state for $k = 0$, and then for the third electron there are four possible ways to occupy one of the orbitals of $k = \pm 2\pi/3$ with the spin $\sigma = \uparrow, \downarrow$. The four-fold degeneracy emerges also for a finite Coulomb interaction $\mathcal{H}_{\text{dot}}^U$, and could cause the SU(4) Kondo behavior.

In the case that one additional electron is introduced into the triangular cluster, the ground state of $\mathcal{H}_{\text{dot}}^0 + \mathcal{H}_{\text{dot}}^U$ for a four-electron occupation $N_{\text{tot}} = 4$ becomes a triplet with the total spin $S = 1$ for $U > 0$ (see also appendix A). This is caused by the Nagaoka ferromagnetic mechanism,⁵⁰ and the energy separation $\Delta E^{(4)} \equiv E_{S=0}^{(4)} - E_{S=1}^{(4)}$ between the ground state $E_{S=1}^{(4)} = U - 2t + 4\epsilon_d$ and the lowest singlet excited state $E_{S=0}^{(4)}$ is given by

$$\Delta E^{(4)} = \frac{1}{2} \left[U + 3t - \sqrt{9t^2 + U^2 + 2Ut} \right]. \quad (7)$$

Note that $\Delta E^{(4)} > 0$ for $U > 0$, and in the two extreme limits at small and large U it takes the form

$$\Delta E^{(4)} \simeq \begin{cases} U/3, & 0 \leq U \ll t \\ t, & 0 < t \ll U \end{cases}. \quad (8)$$

For weak repulsions, an infinitesimal U lifts the degeneracy of the singlet and triplet states in the non-interacting ground state. In the opposite limit, for large U the circular motion along the triangle favors the magnetic $S = 1$ ground state, and the energy separation $\Delta E^{(4)}$ is determined by the hopping matrix element t . If the cluster of the TTQD is connected to the leads, the local magnetic moment will be screened by the conduction electrons showing the two-stage Kondo behavior described in Sec. V.

As the level position ϵ_d decreases further, the occupation number of the electrons increases. The ground-state energy $E_0^{(5)}$ for a five-electron occupation and that for six electrons $E_0^{(6)}$ are given by

$$E_0^{(5)} - E_{S=1}^{(4)} = E_0^{(6)} - E_0^{(5)} = U + t + \epsilon_d. \quad (9)$$

Specifically, at the point where the level in the TTQD ϵ_d takes the value of $\epsilon_d = -U - t$, the ground-state energies for the three different fillings, $N_{\text{tot}} = 4, 5$ and 6, coincide. Thus the occupation number jumps from $N_{\text{tot}} = 4$ to 6, as ϵ_d crosses this value.

C. Phase shifts, conductances & Friedel sum rule

The charge transfer between the dots and leads makes the low-energy states of the whole system a local Fermi liquid, which can be described by renormalized quasi-particles. Particularly, in the case where the system has an inversion symmetry $\Gamma_L = \Gamma_R$, the ground-state properties are characterized by the two phase shifts, δ_e and δ_o , for the quasi-particles with the *even* and *odd* parities. At zero temperature, the series conductance g_s in the two-channel configuration, which is shown in Fig. 1 (a), and the average number of electrons in the triple dots can be expressed, respectively, in the form of a Landauer formula and the Friedel sum rule,^{23,51}

$$g_s = \frac{2e^2}{h} \sin^2 (\delta_e - \delta_o), \quad (10)$$

$$N_{\text{tot}} \equiv \sum_{i=1}^3 \sum_{\sigma} \langle d_{i\sigma}^\dagger d_{i\sigma} \rangle = \frac{2}{\pi} (\delta_e + \delta_o). \quad (11)$$

Furthermore, the parallel conductance g_p for the current flowing along the horizontal direction in the four-terminal geometry, which is shown in Fig. 1 (b), can also be obtained from these two phase shifts

$$g_p = \frac{2e^2}{h} (\sin^2 \delta_e + \sin^2 \delta_o). \quad (12)$$

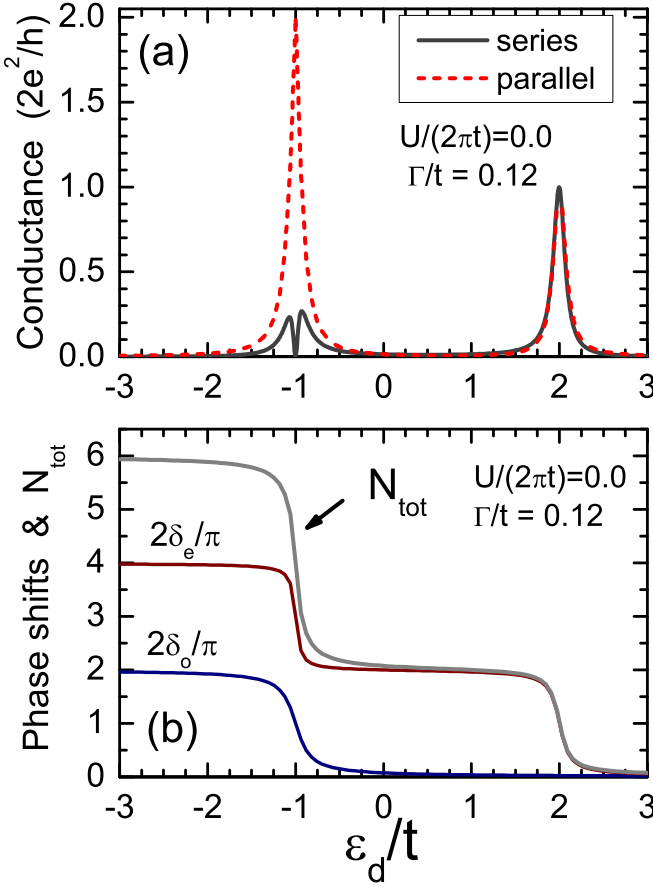


FIG. 2: (Color online) Conductances, phase shifts, and the filling N_{tot} of the triple dot in the non-interacting case $U = 0.0$ are plotted vs ϵ_d/t for a regular triangle $t' = t$, $\epsilon_{\text{apex}} = \epsilon_d$, and $\Gamma/t = 0.12$.

The phase shifts can be expressed in terms of the renormalized matrix element \tilde{t}_{ij} ,^{22,23,24} (see also appendix B)

$$-\tilde{t}_{ij} = -t_{ij} + \epsilon_{d,i} \delta_{ij} + \text{Re } \Sigma_{ij}^+(0), \quad (13)$$

where $\Sigma_{ij}^+(0)$ is the self-energy due to the interaction $\mathcal{H}_{\text{dot}}^U$. Specifically in the inversion symmetric case, the renormalized matrix element \tilde{t}_{ij} for $i, j (= 1, 2, 3)$ inside the TTQD takes the form

$$\{-\tilde{t}_{ij}\} = \begin{bmatrix} \tilde{\epsilon}_d & -\tilde{t} & -\tilde{t}' \\ -\tilde{t} & \tilde{\epsilon}_{\text{apex}} & -\tilde{t} \\ -\tilde{t}' & -\tilde{t} & \tilde{\epsilon}_d \end{bmatrix}, \quad (14)$$

and the two phase shifts are given, respectively, by

$$\cot \delta_e = \frac{\tilde{\epsilon}_d - \tilde{t}' - 2\tilde{t}^2/\tilde{\epsilon}_{\text{apex}}}{\Gamma}, \quad \cot \delta_o = \frac{\tilde{\epsilon}_d + \tilde{t}'}{\Gamma}. \quad (15)$$

As a simple example, the conductances, the phase shifts, and the occupation number N_{tot} in the non-interacting case $\Sigma_{ij}^+ = 0$ are plotted in Fig. 2 as functions of ϵ_d , for $\epsilon_{\text{apex}} = \epsilon_d$, $t' = t$ and $\Gamma/t = 0.12$. We

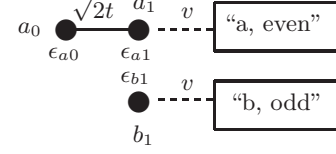


FIG. 3: Even and odd orbitals: the onsite potential of each orbital is given by $\epsilon_{a0} = \epsilon_{\text{apex}}$, $\epsilon_{a1} = \epsilon_d - t'$, and $\epsilon_{b1} = \epsilon_d + t'$.

see in the upper panel (a) that the parallel conductance g_p shows the peaks as the one-particle states defined in Eq. (6) cross the Fermi level, namely at the values of ϵ_d which satisfy $E_k^{(1)} = 0$. We can see that the series conductance g_s has a zero point at $\epsilon_d = -t$. This is due to the destructive interference, which reflects the value of the phase shifts $\delta_e = 3\pi/2$ and $\delta_o = \pi/2$ at this point. The overall ϵ_d dependence of the phase shifts $2\delta_e/\pi$, $2\delta_o/\pi$ and local charge N_{tot} defined in Eq. (11) are shown in the lower panel (b). The phase shifts show a step of the height π as one resonance state crosses the Fermi level. Correspondingly the local charge also shows a staircase behavior. Note that two electrons with spin up and down enter the resonance state simultaneously in the non-interacting case. Among the three one-particle states $k = 0$ and $\pm 2\pi/3$, the lowest one with $k = 0$ is an even-parity state, so that the even phase shift δ_e takes the first step at $\epsilon_d \simeq 2t$. Then at $\epsilon_d \simeq -t$ electrons enter the other two one-particle states which can be classified into an even and odd states.

D. Even and odd orbitals

The non-interacting Hamiltonian $\mathcal{H}_0 \equiv \mathcal{H}_{\text{dot}}^0 + \mathcal{H}_{\text{mix}} + \mathcal{H}_{\text{lead}}$ can be written in a diagonal form, using the even-odd basis

$$a_{1\sigma} \equiv \frac{d_{1\sigma} + d_{3\sigma}}{\sqrt{2}}, \quad b_{1\sigma} \equiv \frac{d_{1\sigma} - d_{3\sigma}}{\sqrt{2}}, \quad (16)$$

and $a_{0\sigma} \equiv d_{2\sigma}$. Here, for the linear combinations the labels 0 and 1 are assigned in the way that is shown in Fig. 3. The couplings to the two leads by Γ breaks the C_{3v} symmetry of the regular triangle, and lift the degeneracy of the even and odd states. In order to see this, we consider the spectral functions defined by

$$A_e(\omega) = -\frac{1}{\pi} \text{Im} \left(\langle\langle a_{0\sigma}; a_{0\sigma}^\dagger \rangle\rangle_\omega + \langle\langle a_{1\sigma}; a_{1\sigma}^\dagger \rangle\rangle_\omega \right), \quad (17)$$

$$A_o(\omega) = -\frac{1}{\pi} \text{Im} \langle\langle b_{1\sigma}; b_{1\sigma}^\dagger \rangle\rangle_\omega, \quad (18)$$

where $\langle\langle \hat{\mathcal{O}}; \hat{\mathcal{P}} \rangle\rangle_\omega \equiv -i \int_0^\infty dt e^{i(\omega + i0^+)t} \langle\{\hat{\mathcal{O}}(t), \hat{\mathcal{P}}\}\rangle$ is the retarded Green's function. These spectral functions for non-interacting electrons, $U = 0$, are plotted in Fig. 4 as functions of ω for $\Gamma/t = 0.12$ and $\epsilon_d = 0.0$. The odd component $A_o(\omega)$ has a single peak at $\omega \simeq t$, and its width

is wider than that of the peak of $A_e(\omega)$ emerging at the same position. This is because on the resonance at $\omega \simeq t$ the spectral weight of $A_e(\omega)$ is dominated by the component of the apex site a_0 , which is situated away from the leads, as shown in Fig. 3. In contrast, $A_o(\omega)$ represents the spectral weight of the level b_1 , which is directly connected to one of the leads. This geometry of the triangle and the two leads in the even-odd basis causes the difference in the peak width. If the level position is lowered from $\epsilon_d = 0.0$ which is the value chosen for Fig. 3, the peaks move towards the left side in the figure. As the two resonance states approach the Fermi energy $\omega = 0$, the third electron enters the odd-resonance state first rather than the even one, because of the difference in the peak width. Then, both the resonance states become singly occupied when the two peaks just reach $\omega = 0$. Correspondingly, the phase shifts take the values $\delta_e = 3\pi/2$ and $\delta_o = \pi/2$, and the series conductance has a dip at $\epsilon_d/t = -1.0$ in Fig. 2.

The interaction Hamiltonian defined in Eq. (3) can be rewritten, using the even-odd basis, in the form

$$\begin{aligned} \mathcal{H}_{\text{dot}}^U = & U n_{a,0\uparrow} n_{a,0\downarrow} + \frac{U}{2} (n_{a,1\uparrow} n_{a,1\downarrow} + n_{b,1\uparrow} n_{b,1\downarrow}) \\ & + \frac{U}{2} \left(\frac{1}{2} n_{a,1} n_{b,1} - 2 \vec{S}_{a,1} \cdot \vec{S}_{b,1} \right) \\ & + \frac{U}{2} \left(a_{1\uparrow}^\dagger a_{1\downarrow}^\dagger b_{1\downarrow} b_{1\uparrow} + b_{1\uparrow}^\dagger b_{1\downarrow}^\dagger a_{1\downarrow} a_{1\uparrow} \right). \end{aligned} \quad (19)$$

Here, $\vec{S}_{a,i} = \sum_{\sigma\sigma'} a_{i\sigma}^\dagger \vec{\sigma}_{\sigma\sigma'} a_{i\sigma'}/2$, $\vec{\sigma}$ the Pauli matrices, $n_{a,i\sigma} = a_{i\sigma}^\dagger a_{i\sigma}$, and $n_{a,i} = \sum_{\sigma} n_{a,i\sigma}$. The operators $n_{b,1\sigma}$ and $\vec{S}_{b,1}$ for the odd orbital $b_{1\sigma}$ are defined in the same way. We see in Eq. (19) that the interaction contains some long-range components between a_1 and b_1 orbitals. Specifically, the last two terms in the right hand side describe a charge transfer which breaks the charge conservation in each of the even and odd channels. Thus for $U \neq 0$, each of the phase shifts δ_e and δ_o does not necessarily correspond, respectively, to $\langle n_{a,0} + n_{a,1} \rangle \pi/2$ and $\langle n_{b,1} \rangle \pi/2$. The Friedel sum rule given in Eq. (11) holds in a way such that $\delta_e + \delta_o = \langle n_{a,0} + n_{a,1} + n_{b,1} \rangle \pi/2$.

III. LOW-ENERGY SU(4) SYMMETRY AT ZERO POINTS OF CONDUCTANCE

In this section we show that the low-lying excitations acquire a special symmetry between channels at the zero points of the series conductance. This is a general property of a Fermi-liquid fixed point for a quantum-impurity system connected to two conduction channels. To be specific, we consider the case that the system has time-reversal and inversion symmetries. We use the discretized Hamiltonian H_N of NRG^{52,53} (see also appendix C) in this section not for a numerical purpose, but for showing explicitly the symmetric properties that emerge in a finite-size spectrum.

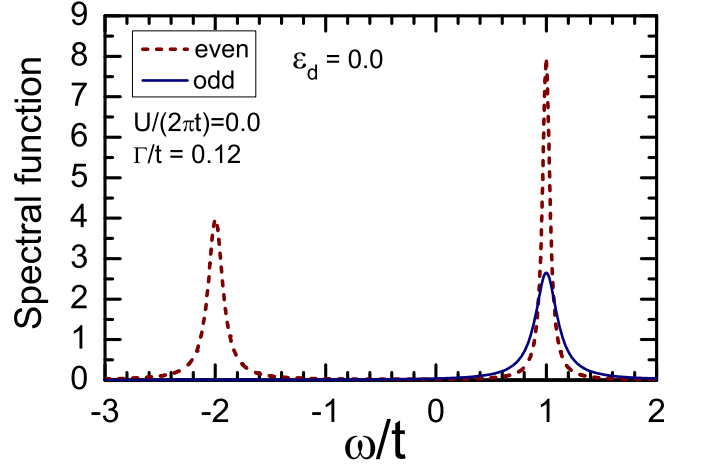


FIG. 4: (Color online) Spectral functions $A_e(\omega)$ and $A_o(\omega)$ for non-interacting electrons $U = 0.0$, for $\epsilon_d = 0.0$, $t' = t$, $\epsilon_{\text{apex}} = \epsilon_d$, and $\Gamma/t = 0.12$. The even and odd components are defined in Eqs. (16)–(18).

The two phase shifts δ_e and δ_o for interacting electrons can be deduced from the fixed-point eigenvalues of the discretized Hamiltonian H_N defined in Eq. (C1), following the procedure described in Ref. 23. Conversely, for some particular values of the phase shifts, one can deduce that the system captures a special symmetry asymptotically at low energies. Particularly at the zero points of the series conductance, the low-lying energy spectrum for the even (*s*-wave) and odd (*p*-wave) channels become identical near the Fermi energy. It means that the quasi-particles of the local Fermi liquid acquire the channel degeneracy as well as the spin degeneracy.

In order to see this, we go back briefly to a few essential points of the NRG. At a Fermi-liquid fixed point the low-lying energy spectrum of the many-body Hamiltonian H_N defined in (C1) can be reproduced by a discretized version of free quasi-particle Hamiltonian $H_{\text{eff}}^{(N)}$,

$$\begin{aligned} H_{\text{eff}}^{(N)} &\equiv \Lambda^{(N-1)/2} \left(\tilde{\mathcal{H}}_{\text{dot}} + H_{\text{mix}} + H_{\text{lead}}^{(N)} \right) \\ &= \sum_{\sigma=\uparrow,\downarrow} \sum_{\mu=e,o} \sum_l \varepsilon_{l\mu}^{(N)} \gamma_{l,\mu\sigma}^\dagger \gamma_{l,\mu\sigma}. \end{aligned} \quad (20)$$

Here, the renormalized TTQD part, $\tilde{\mathcal{H}}_{\text{dot}}$, in the first line is defined in Eq. (B6). The second line is a diagonal form, for which μ ($= e, o$) is the channel index, and the label l is a quantum number for the eigenstates in each channel. The ground state for $H_{\text{eff}}^{(N)}$ can be constructed in a such way that all the states for $\varepsilon_{l\mu}^{(N)} < 0$ are filled by the $\gamma_{l,\mu\sigma}$ particles, and the excitation energy $\varepsilon_{l\mu}^{(N)}$ of the quasi-particles near the Fermi level can be determined from the fixed-point eigenvalues of H_N .^{52,53}

The phase shifts can be expressed as $\kappa_\mu = -\cot \delta_\mu$ in terms of the parameter κ_μ which determines the value of a Green's function at the Fermi energy, as shown in Eq. (B8). The value of this parameter κ_μ can be deduced

from the quasi-particle energy spectrum $\varepsilon_{l\mu}^{(N)}$,²³

$$\kappa_\mu = \frac{2A_\Lambda}{\pi} \lim_{N \rightarrow \infty} D \Lambda^{(N-1)/2} g_N(\varepsilon_{l\mu}^{(N)}). \quad (21)$$

Here, A_Λ is a coefficient which is defined in (C4), D is the half width of the conduction band, and $g_N(\varepsilon)$ is a local Green's function at the interface $n = 0$ of the discretized version of the non-interacting lead $H_{\text{lead}}^{(N)}$ given in (C3). The equation (21) represents the relation between the phase shift and the low-energy quasi-particle spectrum in each channel μ . The right hand side of Eq. (21) converges to the same value of κ_μ for any l , as long as $\varepsilon_{l\mu}^{(N)}$ is an excitation energy near the Fermi energy of the quasi-particles $\gamma_{l,\mu\sigma}$. Specifically, it is not necessary that $\varepsilon_{l\mu}^{(N)}$ should be the lowest excitation energy, although the lowest one is preferable for a numerical purpose to make the corrections due to a residual interaction between the quasi-particles small.⁵⁴

One can deduce conversely the properties of the low-energy spectrum from the values of κ_e and κ_o , using Eq. (21). Particularly at zero points of the series conductance, the phase shifts satisfy the condition $\delta_e - \delta_o = n\pi$ for $n = 0, \pm 1, \pm 2, \dots$. This is equivalent to $\kappa_e = \kappa_o$, and thus from Eq. (21) it is deduced that the low-lying energy spectrum for the even and odd channels become identical for large N , namely $\varepsilon_{l,e}^{(N)} = \varepsilon_{l,o}^{(N)}$ for all l near the Fermi level of the quasi-particles. Thus the quasi-particles acquire a rotational symmetry in the channel (flavor) space asymptotically at low energies, in addition to the rotation symmetry of the spin. Therefore, $H_{\text{eff}}^{(N)}$ has a $\text{SU}(4)$ symmetry at the zero points of the series conductance.

In the special case $\kappa_e = 0$ and $\kappa_o = 0$, which correspond to $\delta_e = (n + 1/2)\pi$ and $\delta_o = (n' + 1/2)\pi$ for integer n and n' , the low-lying energy states have a particle-hole symmetry in addition to the channel symmetry, because the lead Green's function in the right hand side of Eq. (21) is an odd function of the frequency $g_N(-\varepsilon) = -g_N(\varepsilon)$, due to the particle-hole symmetry of $H_{\text{lead}}^{(N)}$.

There are some other interesting cases in the unitary limit, at which the series conductance reaches $g_s = 2e^2/h$. If the two phase shifts take the values of $\delta_e = (n \pm 1/4)\pi$ and $\delta_o = (n' \mp 1/4)\pi$, then κ_μ becomes $\kappa_e = \mp 1$ and $\kappa_o = \pm 1$. Therefore in this case the low-energy excitations acquire a particle-hole symmetry between a particle (hole) in the even channel and a hole (particle) in the odd channel, although there is no channel symmetry in this case. It can also be deduced from Eq. (21) that for the other set of the phase shifts, $\delta_e = (n + 1/2)\pi$ and $\delta_o = n'\pi$, particle-hole symmetry holds in each channel at low energies.

IV. GROUND-STATE PROPERTIES

We have carried out the NRG calculations in order to study the effects of the interaction on the transport

and magnetic properties. Specifically we concentrate on the regular triangle case, for which $\epsilon_d = \epsilon_{\text{apex}}$ and $t' = t$ in the following. We will examine the effects of the deformations of the regular triangle caused by ϵ_{apex} and t' in Sec. VI.

The ratio of the inter-dot hopping matrix element t and the half width of the conduction band D are chosen typically to be $t/D = 0.1$ in most of our calculations. The iterative diagonalization has been carried out by using the even-odd basis. For constructing the Hilbert space at each NRG step, instead of adding two orbitals from even and odd orbitals simultaneously, we add the one from the even part first and retain 3600 low-energy states after carrying out the diagonalization of the Hamiltonian. Then, we add the other orbital from the odd part, and again keep the lowest 3600 eigenstates after the diagonalization. This truncation procedure preserves the inversion symmetry. We have chosen the discretization parameter to be $\Lambda = 6.0$. It has been confirmed that the conductance for noninteracting electrons $U = 0$ is reproduced sufficiently well with this calculation scheme.^{22,23,24}

A. Results at a small Γ and large U

The phase shifts and conductances for a relatively weak coupling $\Gamma/t = 0.12$ and strong interaction $U/(2\pi t) = 1.0$ are plotted as functions of ϵ_d/U in Fig. 5. The number of electrons N_{tot} in the triangle increases with decreasing ϵ_d . It shows plateaus for $N_{\text{tot}} = 1, 2, 3$ and 4, and then jumps to $N_{\text{tot}} \simeq 6.0$ at $\epsilon_d \simeq -1.16U$ without taking a step for $N_{\text{tot}} \simeq 5.0$. The same behavior has already been seen in the case of the triangular cluster, for which the ground-states energies for the three different fillings, $N_{\text{tot}} = 4, 5$ and 6, coincide at $\epsilon_d = -t - U$, as mentioned in Sec. II B. The vertical dashed lines in (a) correspond to the values of ϵ_d at which the local charge varies discontinuously in the limit of $\Gamma = 0$. We can see that the staircase behavior of N_{tot} in this small Γ case is essentially determined by the one in this isolated limit.

The triangular triple dot has the $S = 1$ local moment due to the Nagaoka ferromagnetic mechanism at the plateau for $N_{\text{tot}} \simeq 4.0$, as mentioned in Sec. II A. This moment is screened at low temperatures by the conduction electrons from the two leads, and the ground state of the whole system becomes a singlet. We can see in Fig. 5(b) that the two conductances show a significant difference at this filling $N_{\text{tot}} \simeq 4.0$. At $-1.15U \lesssim \epsilon_d \lesssim -0.85U$ the parallel conductance reaches the unitary limit of two conducting channels $g_p \simeq 4e^2/h$, while the series conductance g_s is suppressed. We have seen a similar difference between g_p and g_s for $U = 0$ near the peaks at $\epsilon_d = -t$ in Fig. 2 (a). We can see in Fig. 5 (a) that the two phase shifts are locked at the value $\delta_e \simeq 3\pi/2$ and $\delta_o \simeq \pi/2$ in the wide region $-1.15U \lesssim \epsilon_d \lesssim -0.85U$, due to the Coulomb interaction. Therefore in this region, both the even and odd channels give a unitary-limit contribution to the four-terminal conductance g_p , while the destruc-

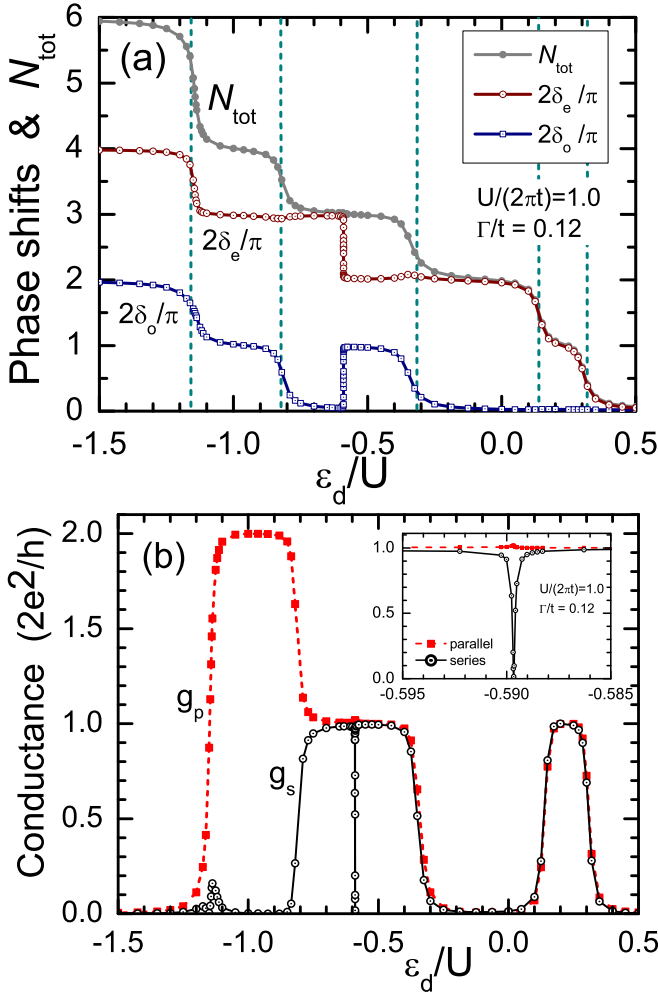


FIG. 5: (Color online) Plots of NRG results as functions of ϵ_d/U for $U/(2\pi t) = 1.0$, $\Gamma/t = 0.12$, $t' = t$ and $\epsilon_{\text{apex}} = \epsilon_d$. (a): the local charge N_{tot} , the phase shifts $2\delta_e/\pi$ and $2\delta_o/\pi$. (b): the series (\odot) and parallel (\blacksquare) conductances. The vertical dashed lines in (a) correspond to ϵ_d , at which N_{tot} in the limit of $\Gamma = 0$ varies discontinuously. At the zero point of the series conductance for $\epsilon_d \simeq -0.59U$, the phase shifts take the values $\delta_o \simeq \pi/4$ and $\delta_e \simeq 5\pi/4$. Inset in (b) shows the region near the zero point of g_s .

tive interference reduces the two terminal conductance g_s .

The difference between the two phase shifts $\delta_e - \delta_o$ is shown in Fig. 6. It crosses the value of π at $\epsilon_d/U \simeq -1.15$, -0.88 and -0.59 . At these three points the series conductance becomes zero. The series conductance must have a maximum between two adjacent zero points, and thus a fine structure of g_s seen at $-1.2U \lesssim \epsilon_d \lesssim -1.1U$ can be regarded as one such example. It should be noted that in the non-interacting case only a single zero point appears as ϵ_d varies (see Fig. 2 (a)).

In most of the other regions of the electron filling, the series and parallel conductances show a similar ϵ_d dependence. For instance, both the two conductances show a plateau with the value $2e^2/h$ for $0.15U \lesssim \epsilon_d \lesssim 0.3U$ in

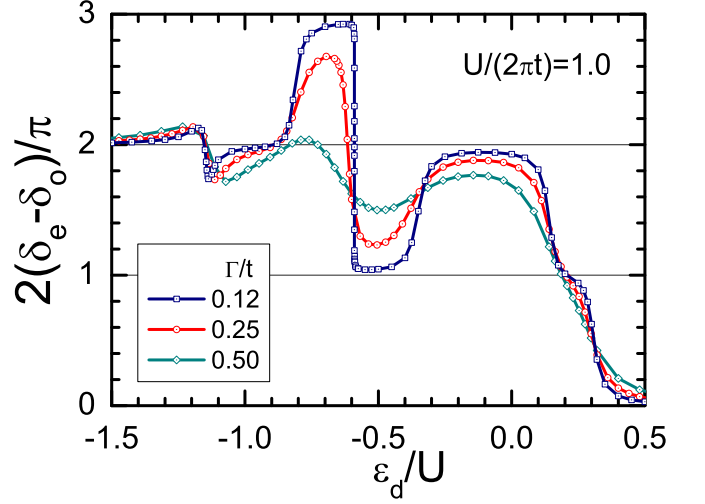


FIG. 6: (Color online) Difference between the two phase shifts $2(\delta_e - \delta_o)/\pi$ is plotted vs ϵ_d/U for $U/(2\pi t) = 1.0$, for several values of Γ/t (\square) 0.12 (\odot) 0.25, and (\diamond) 0.5. At the points where the lines cross the horizontal line of $\delta_e - \delta_o = \pi$, the series conductance g_s becomes zero.

Fig. 5(b). This Kondo behavior is caused by a $S = 1/2$ moment of a single electron which occupies the lowest even-parity orbital with the energy $E_{k=0}^{(1)}$. Then, for $-0.3U \lesssim \epsilon_d \lesssim 0.1U$, two electrons fill the lowest orbital, and both the series and parallel conductances are suppressed. As ϵ_d decreases further, for $-0.58U \lesssim \epsilon_d \lesssim -0.3U$, the third electron enters the odd orbital corresponding to the site b_1 which is illustrated in Fig. 3. The moment due to the third electron causes the $SU(2)$ Kondo effect in this region.

We can see in Fig. 5(b) that there is a sharp dip in the series conductance at $\epsilon_d \simeq -0.59U$ in the middle of the plateau for $N_{\text{tot}} \simeq 3.0$. This reflects a sudden change of the two phase shifts, seen in Fig. 5(a). Near the series conductance dip, the difference between the two phase shifts $\delta_e - \delta_o$ varies from $\pi/2$ to $3\pi/2$ continuously, taking the middle value of π at the zero point of g_s . In contrast, the sum of the two phase shifts does not show a significant change, and is almost a constant $\delta_e + \delta_o \simeq 3\pi/2$ which corresponds to the occupation number $N_{\text{tot}} \simeq 3.0$. Thus the parallel conductance varies very little in this narrow region, keeping the value $g_p \simeq 2e^2/h$. Furthermore, the two phase shifts take the value $\delta_o \simeq \pi/4$ and $\delta_e \simeq 5\pi/4$ at the zero point of g_s in the center of the dip. These values of the phase shifts are consistent with the one reported for a capacitively coupled double dot with a single electron in an $SU(4)$ symmetric limit.⁴⁶ As mentioned in Sec. III, the quasi-particle excitations have channel degeneracy as well as the spin degeneracy generally at zero points of the series conductance, and the system has an $SU(4)$ symmetry of a Fermi-liquid origin at low energies. In the case of the TTQD, the system also has an $SU(4)$ symmetry of a different origin at high energies, which is caused by the four-fold degenerate eigenstates of the iso-

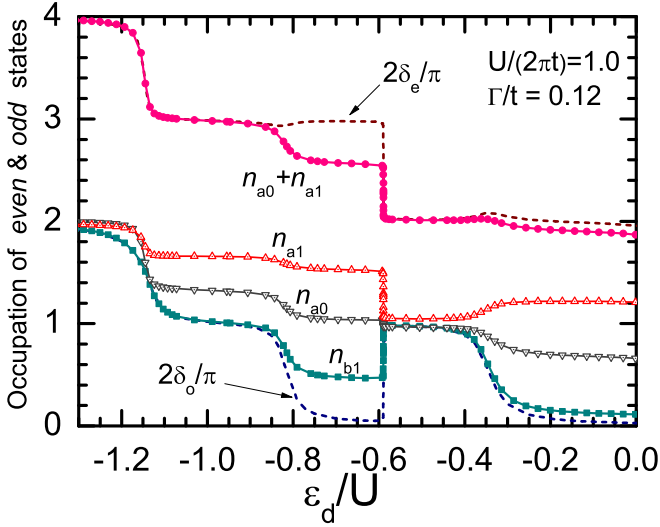


FIG. 7: (Color online) Filling of even and odd orbitals, $\langle n_{a,0} \rangle$, $\langle n_{a,1} \rangle$ and $\langle n_{b,1} \rangle$ are plotted vs ϵ_d/U for $U/(2\pi t) = 1.0$ and $\Gamma/t = 0.12$. The dashed lines correspond to the phase shifts $2\delta_e/\pi$ and $2\delta_o/\pi$. Just at the zero point, $\epsilon_d \simeq -0.59U$, of the series conductance in the middle of the crossover region the phase shifts take the values $\delta_o \simeq \pi/4$, $\delta_e \simeq 5\pi/4$, and three electrons distribute in these orbitals as $\langle n_{a,0} \rangle \simeq 1.0$, $\langle n_{a,1} \rangle \simeq 1.28$, and $\langle n_{b,1} \rangle \simeq 0.72$.

lated triangular cluster with three electrons, mentioned in Sec. II B. We will see in Sec. V from the results of the thermodynamic quantities that the four-fold degenerate local degrees of freedom remain free at high temperatures, and are screened at low temperatures by the conduction electrons keeping the SU(4) symmetric behavior.

The sudden change of the two phase shifts also implies that a charge redistribution takes place in the TTQD. One might expect from the behavior of δ_e and δ_o that the third electron moves away from the odd orbital to enter the second even orbital for $-0.8U \lesssim \epsilon_d \lesssim -0.6U$. Each of the two phase shifts, however, does not necessarily correspond to the occupation number of the orbitals of each parity, $N_{\text{even}} \equiv \langle n_{a,0} + n_{a,1} \rangle$ or $N_{\text{odd}} \equiv \langle n_{b,1} \rangle$, in the interacting case $U \neq 0$, as mentioned in Sec. II D. For this reason, we have calculated also the expectation value of $\langle n_{a,i} \rangle$ and $\langle n_{b,1} \rangle$ with the NRG in order to clarify precisely the charge distribution. The results are presented in Fig. 7. We see that an intuitive estimate, which assumes $N_{\text{even}} \approx 2\delta_e/\pi$ and $N_{\text{odd}} \approx 2\delta_o/\pi$, approximately works for $\epsilon_d \lesssim -0.85U$ and $-0.6U \lesssim \epsilon_d$. For instance, the third electron really enters into the odd orbital to take the occupation number of the value, $\langle n_{b,1} \rangle \simeq 1.0$, for $-0.58U \lesssim \epsilon_d \lesssim -0.4U$ on the right side of the series conductance dip. Such a separation of the Friedel sum rule, however, does not make sense in the central region. We can see for $-0.75 \lesssim \epsilon_d/U \lesssim -0.6$ that the local charges are redistributed between the even and odd orbitals, and take the values $\langle n_{a,0} \rangle \simeq 1.0$, $\langle n_{a,1} \rangle \simeq 1.5$, and $\langle n_{b,1} \rangle \simeq 0.5$. Thus $N_{\text{even}} \simeq 2.5$ and $N_{\text{odd}} \simeq 0.5$, while the

phase shifts take the values $2\delta_e/\pi \simeq 3.0$ and $2\delta_o/\pi \simeq 0.0$. Furthermore, at the zero point of the series conductance the phase shifts take the values $\delta_o \simeq \pi/4$ and $\delta_e \simeq 5\pi/4$ as mentioned, while the occupation number for the even and odd orbitals become $\langle n_{a,0} \rangle \simeq 1.0$, $\langle n_{a,1} \rangle \simeq 1.28$, and $\langle n_{b,1} \rangle \simeq 0.72$.

The charge distribution in real space can also be deduced, using the operator identities $n_{d,2} \equiv n_{a,0}$ and $n_{d,1} + n_{d,3} = n_{a,1} + n_{b,1}$ which follow from the definition in (16),

$$\langle n_{d,1} \rangle = \langle n_{d,3} \rangle = \langle n_{a,1} + n_{b,1} \rangle / 2. \quad (22)$$

We have confirmed that the numerical value of $\langle n_{a,0} \rangle$ and $\langle n_{a,1} + n_{b,1} \rangle / 2$ are very close in the whole region of ϵ_d plotted in Fig. 7. Thus the occupation number of the apex site, $\langle n_{d,2} \rangle$, is not much different from $\langle n_{d,1} \rangle$, or $\langle n_{d,3} \rangle$. Consequently, for small Γ , the charge distribution is almost homogeneous in real space. The charge inhomogeneity in the even-odd basis, however, affects the transport and magnetic properties very much. This is because the orbitals a_1 and b_1 are connected directly to the leads as shown in Fig. 3, while the apex site does not have a direct connection to the leads.

We can see also at $-1.15U \lesssim \epsilon_d \lesssim -0.83U$ in Fig. 7 that four electrons in the TTQD are distributed in the even and odd orbitals such that $\langle n_{a,0} \rangle \simeq 1.3$, $\langle n_{a,1} \rangle \simeq 1.7$, and $\langle n_{b,1} \rangle \simeq 1.0$. These values are close, respectively, to $4/3$, $5/3$ and 1 , which are the occupation numbers in the cluster limit $\Gamma = 0$ (see appendix A).

B. Large Γ cases

The conductances and phase shifts discussed in the above are the results obtained for a relatively small hybridization $\Gamma/t = 0.12$. For this reason the structures of the plateaus and valleys can be seen very clearly. We next examine how the strength of the couplings Γ between the triangle and two leads affects the ground-state properties. For comparison with the data shown in Fig. 5, we have carried out the calculations for several larger values of Γ keeping the interaction U the same value of $U/(2\pi t) = 1.0$. The results are shown in Fig. 8. The couplings are chosen such that $\Gamma/t = 0.25$ for (a) and (b), and $\Gamma/t = 0.5$ for (c) and (d).

As a general trend, the structures seen in the phase shifts and conductances are smeared gradually as the couplings get stronger. We see in the upper panels (a) and (b) of Fig. 8, however, that the structures are still distinguishable by eye in the case of $\Gamma/t = 0.25$, and the feature of each line can be compared with the corresponding line in Fig. 5. Specifically, for $N_{\text{tot}} \simeq 3.0$ the broadening makes the dip of the series conductance near $\epsilon_d \simeq -0.6U$ wider. This structure reflects the behavior of the phase shifts at $-0.8U \lesssim \epsilon_d \lesssim -0.6U$ in Fig. 8 (a). In this region the odd phase shift δ_o still shows a clear concaving valley, although it becomes shallower than that in the case of Fig. 5 (a). This valley is smeared further

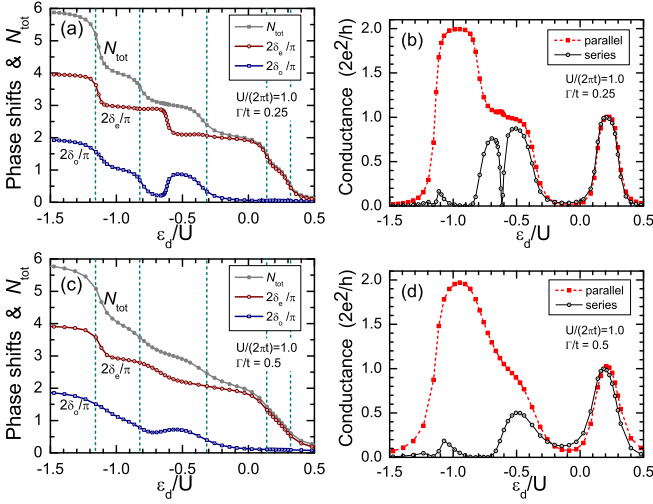


FIG. 8: (Color online) Phase shifts and conductances for large hybridizations (upper panels) $\Gamma/t = 0.25$ and (lower panels) $\Gamma/t = 0.5$; $U/(2\pi t) = 1.0$ is fixed. The vertical dashed lines in (a) and (c) correspond to ϵ_d , at which N_{tot} in the limit of $\Gamma = 0$ varies discontinuously.

in the case of $\Gamma/t = 0.5$, and the fine structure of g_s at $-0.8U \lesssim \epsilon_d \lesssim -0.6U$ is not visible in Fig. 8 (d). Particularly, the conductance plateau on the left side of the dip almost vanishes. We can see, nevertheless, in Fig. 6 that the difference between the two phase shifts $\delta_e - \delta_o$ for $\Gamma/t = 0.5$ crosses the value of π at $\epsilon_d/U \simeq -0.73$, -0.82 , and -1.15 . It means that there still exist three zero points of the series conductance, and g_s has a weak maximum between the two adjacent zero points.

In contrast to the series conductance g_s , the parallel conductance g_p is less sensitive to Γ . Particularly, we can see that in Fig. 8 that the broad peaks of g_p at $N_{\text{tot}} \simeq 4.0$ and $N_{\text{tot}} \simeq 1.0$ keep their essential features seen in the small Γ case in Fig. 5. This is because the energy gain of the Nagaoka state $\Delta E^{(4)}$, which is defined in Eq. (7), is of the order of the inter-dot hopping matrix element t for large U . It takes a value of $\Delta E^{(4)}/t = 0.735$ for $U/(2\pi t) = 1.0$, and thus in the present case $\Delta E^{(4)}/t$ is still much larger than the energy scale of the hybridization $\Gamma/t = 0.5$.

We can also see another quantitative change in Fig. 8 (d) that the difference between g_p and g_s at $N_{\text{tot}} \simeq 1.0$ becomes visible for large Γ . A similar tendency was seen also for the conductances of a linear triple dot.²³

C. Small U cases

We next consider the ground-state properties for weak interactions. For comparison with the case of Fig. 5, we have carried out the calculations, taking U smaller than $U/(2\pi t) = 1.0$ and choosing the same value of $\Gamma/t = 0.12$ for the hybridization. The results are plotted in Fig. 9; the upper panels (a)–(b) for $U/(2\pi t) = 0.5$, and the lower

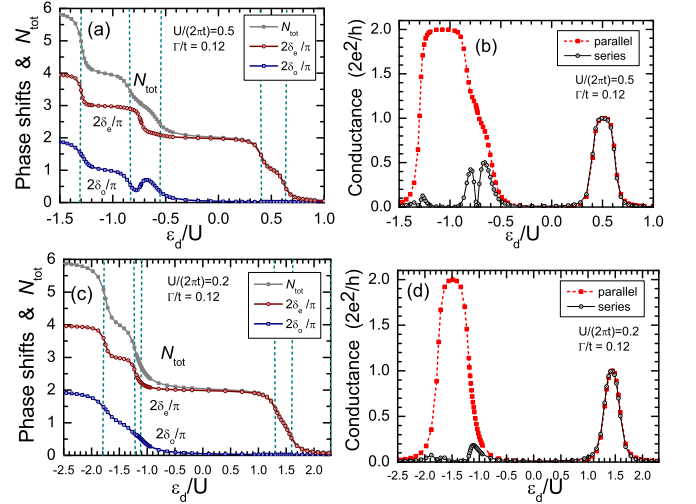


FIG. 9: (Color online) Phase shifts and conductances for small values of U (upper panels) $U/(2\pi t) = 0.5$ and (lower panels) $U/(2\pi t) = 0.2$; $\Gamma/t = 0.12$ is fixed. The vertical dashed lines in (a) and (c) correspond to ϵ_d , at which N_{tot} for $\Gamma = 0$ varies discontinuously.

panels (c)–(d) for $U/(2\pi t) = 0.2$. The vertical dashed lines in the panels (a) and (c), show the values of the ϵ_d at which the occupation number N_{tot} changes in the isolated limit $\Gamma = 0$.

We can see that the area for three-electron filling becomes broad as U increases. Note that in the non-interacting case the occupation number N_{tot} does not take the steps at $N_{\text{tot}} \simeq 1.0$, 3.0 and 4.0 as shown in Fig. 2(b). Therefore the effects of the Coulomb interaction are particularly important for these electron fillings. The conductance peak at $N_{\text{tot}} \simeq 1.0$ becomes wider as U increases, and the peak shape deviates from a simple Lorentzian form which is seen in Fig. 2(b) for $U = 0$. This is caused by the SU(2) Kondo effects due to the moment of a single electron occupying the local one-particle state $E_{k=0}^{(1)}$ in the triangle, as mentioned.

We see in (a) and (b) of Fig. 9 that the overall feature of the phase shifts and the conductances for $U/(2\pi t) = 0.5$ are similar to the those for $U/(2\pi t) = 1.0$ shown in Fig. 5. For instance, the dip structure of the series conductance is clearly seen for $N_{\text{tot}} \simeq 3.0$ in (b), which reflects the behavior of the phase shifts at $-0.8 \lesssim \epsilon_d/U \lesssim -0.6$ in Fig. 9 (a). Particularly, the peak of g_s on the left side of the dip is caused by a concaving behavior of δ_o . The occupation number N_{tot} , however, no longer shows a clear staircase behavior at three-electron filling for $U/(2\pi t) = 0.5$. Correspondingly, we see in Fig. 9 (b) that the parallel conductance g_p has a shoulder behavior, instead of a well-defined plateau, at $-0.8 \lesssim \epsilon_d/U \lesssim -0.6$.

These plateau and valley structures almost disappear for the smaller interaction $U/(2\pi t) = 0.2$, as shown in the lower panels (c) and (d) of Fig. 9. Specifically, the region for three-electron filling, which corresponds to $-1.2 \lesssim \epsilon_d/U \lesssim -1.1$, becomes very narrow, as men-

tioned. Nevertheless, we have confirmed that the difference between the two phase shifts $\delta_e - \delta_o$ crosses the value of π at the points $\epsilon_d/U \simeq -1.2, -1.4$ and -1.7 , which correspond to the zero points of g_s . The series conductance has a weak peak between the two adjacent zero points, although it is not visible on the scale of Fig. 9.

The parallel conductance at four-electron filling, which is shown in (b) and (d) of Fig. 9, keeps the features of the $S = 1$ Kondo behavior seen for larger U in Fig. 5. This is because the Coulomb interaction is still larger than the inter-dot hopping matrix element t , even for $U/(2\pi t) = 0.2$. Correspondingly, we can see in Fig. 9 (c) that the even phase shift shows a clear plateau behavior for $\delta_e \simeq 3\pi/2$ at $-1.7 \lesssim \epsilon_d/U \lesssim -1.3$, although the odd phase shift δ_o behaves moderately. Note that the energy gain of the Nagaoka state is given by $\Delta E^{(4)} = 0.319t$ for $U/(2\pi t) = 0.2$, and $\Delta E^{(4)} = 0.563t$ for $U/(2\pi t) = 0.5$. Therefore, in both of these two cases the energy $\Delta E^{(4)}$ is greater than Γ ($= 0.12t$), and it makes the $S = 1$ Kondo behavior robust.

V. THERMODYNAMIC QUANTITIES

We present the NRG results for the magnetic susceptibility and the entropy of the TTQD in this section. The Kondo behavior in a wide energy scale can be investigated from the temperature dependence of these thermodynamic quantities. Particularly, we study how the screening of the local moment is completed in the case of the $S = 1$ high-spin Nagaoka state at $N_{\text{tot}} \simeq 4.0$. We investigate also the $SU(4)$ Kondo behavior, which takes place at the series conductance dip in the middle of the plateau at $N_{\text{tot}} \simeq 3.0$.

A. Entropy & spin susceptibility

The free energy of the whole system consisting of the dots and leads is given by $F = -T \log [\text{Tr} e^{-\mathcal{H}/T}]$. The contribution of the quantum dots on this free energy can be extracted, by subtracting the contribution of the non-interacting leads, $F_{\text{lead}} = -T \log [\text{Tr} e^{-\mathcal{H}_{\text{lead}}/T}]$, from the total free energy,⁵²

$$\Delta F \equiv F - F_{\text{lead}}. \quad (23)$$

Then, the entropy \mathcal{S} and the spin susceptibility χ due to the dots can be obtained from

$$\mathcal{S} \equiv -\frac{\partial \Delta F}{\partial T}, \quad \chi \equiv -\frac{\partial^2 \Delta F}{\partial H^2}. \quad (24)$$

Here, the magnetic field H is introduced both for the dots and leads, adding the Zeeman energy \mathcal{H}_{ex} to the

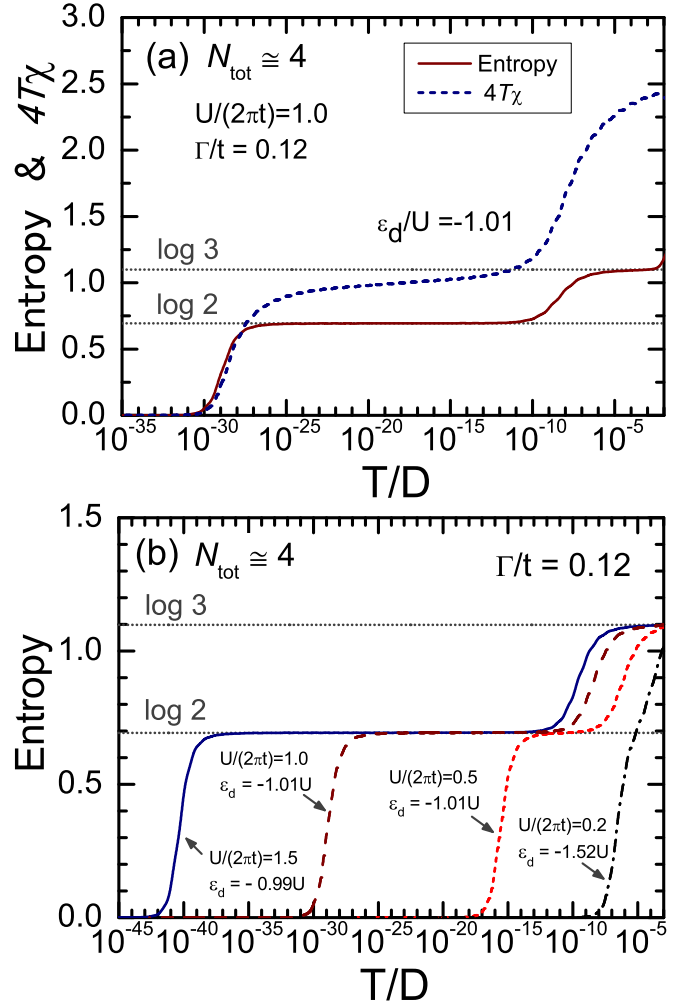


FIG. 10: (Color online) Entropy \mathcal{S} and spin susceptibility $4T\chi$ in the middle of the charge step for $N_{\text{tot}} \simeq 4.0$ are plotted vs $\log(T/D)$ for $t' = t$, $\epsilon_{\text{apex}} = \epsilon_d$ and $\Gamma/t = 0.12$, where D the half-width of the conduction band. In (a) both \mathcal{S} and $4T\chi$ are plotted for $U/(2\pi t) = 1.0$ and $\epsilon_d = -1.01U$. In (b) entropy is plotted for several values of U : (dash-dot line) $U/(2\pi t) = 0.2$, $\epsilon_d = -1.52U$, (dotted line) $U/(2\pi t) = 0.5$, $\epsilon_d = -1.01U$, (dashed line) $U/(2\pi t) = 1.0$, $\epsilon_d = -1.01U$, and (solid line) $U/(2\pi t) = 1.5$, $\epsilon_d = -0.99U$.

Hamiltonian \mathcal{H} defined in Eq. (1),

$$\begin{aligned} \mathcal{H}_{\text{ex}} = & - \sum_{i=1}^3 (n_{d,i\uparrow} - n_{d,i\downarrow}) H \\ & - \sum_{\nu=L,R} \sum_k \left(c_{k\nu\uparrow}^\dagger c_{k\nu\uparrow} - c_{k\nu\downarrow}^\dagger c_{k\nu\downarrow} \right) H. \end{aligned} \quad (25)$$

These thermodynamic quantities can be evaluated using the eigenvalues of the discretized Hamiltonian of the NRG.⁵²

B. Screening of $S = 1$ Nagaoka high spin

The entropy \mathcal{S} and $4\chi T$ are plotted in Fig. 10 (a) as functions of $\log(T/D)$ for a parameter set, $U/(2\pi t) = 1.0$ and $\epsilon_d = -1.01U$, which corresponds to the middle of the charge step for $N_{\text{tot}} \simeq 4.0$ in Fig. 5. We can see that the screening of the spin $S = 1$ local moment is achieved via two separate stages. The first and second stages take place at $T/D \simeq 10^{-8}$ and $T/D \simeq 10^{-29}$, respectively. At high temperatures $10^{-7} \lesssim T/D \lesssim 10^{-3}$, the entropy shows a plateau of the value of $\mathcal{S} \simeq \log 3$, which represents the contribution of a free unscreened $S = 1$ moment. Then, at intermediate temperatures $10^{-27} \lesssim T/D \lesssim 10^{-10}$, the entropy takes the other value $\mathcal{S} \simeq \log 2$ corresponding to a spin $1/2$ moment. In this region, the spin susceptibility also shows a Curie behavior $4\chi T \simeq 1.0 \Rightarrow 4s(s+1)/3$ with a coefficient $s = 1/2$ due to a free spin. Therefore in the intermediate temperature region, half of the $S = 1$ moment is screened by the conduction electrons from one of the channel degrees of freedom, and the local moment is still in an under-screened situation with the remaining free spin of $s = 1/2$. The full screening is completed at low temperature of the order $T/D \simeq 10^{-30}$ in the case of Fig. 10 (a). This crossover energy scale to the low-energy Fermi-liquid regime can be regarded as a Kondo temperature for the $S = 1$ local moment in the present case. We refer to the crossover energy scale to the singlet ground state as the screening temperature T^* , and use this definition for a wide range of electron filling $0 < N_{\text{tot}} < 6$.

The reason that the two stages are required to reach the Kondo singlet state can be understood from the distribution of the $S = 1$ moment in the triangular triple dot. Specifically in the limit of $\Gamma = 0$, the partial moment $m_{a/b,i}$, which constitutes the $S = 1$ moment as shown in appendix A, distributes in the even-odd orbitals a_0 , a_1 and b_1 with the weights $1/3$, $1/6$, and $1/2$, respectively. Among the three orbitals, a_1 and b_1 are coupled directly to the lead, as illustrated in Fig. 3. Therefore, the partial moments in these two orbitals can be screened directly by the conduction electrons at the first stage. In contrast, the other orbital a_0 has no direct tunneling matrix element to the leads, and thus the partial moment in the a_0 orbital has to be screened indirectly by the conduction electrons coming over the a_1 orbital which is already filled up to $\langle n_{a,1} \rangle \simeq 1.7$, as mentioned in IV A. This amount of the occupation number is caused mainly by the difference between the onsite potential $\epsilon_{a0} = \epsilon_d$ and $\epsilon_{a1} = \epsilon_d - t$ in the even-odd basis, namely ϵ_{a1} is deeper than ϵ_{a0} (see also appendix A). Therefore, in this situation the charge and spin fluctuations must be nearly frozen in the a_1 orbital, and the screening temperature for the partial moment in the apex site a_0 becomes low. These features of the screening at the second stage are analogous to those of a super-exchange mechanism.

We see in Fig. 10 (a) that the essential feature of the screening can be observed either in \mathcal{S} or $T\chi$. At the transient regions, however, \mathcal{S} varies more clearly than

$T\chi$ does. Therefore, in order to see how the Coulomb interaction U affects the two-stage screening of the $S = 1$ moment at $N_{\text{tot}} \simeq 4.0$, the entropy \mathcal{S} is plotted in Fig. 10 (b) for several values of U , choosing the parameter set $(U/(2\pi t), \epsilon_d/U)$ in a way such that it corresponds to the middle of the plateau of the parallel conductance, solid line: $(1.5, -0.99)$, dashed line: $(1.0, -1.01)$, dotted line: $(0.5, -1.01)$, and dash-dot line: $(0.2, -1.52)$. The hybridization is chosen to be $\Gamma/t = 0.12$. Note that the ground-state properties for these two small U cases were presented in Fig. 9. We see in Fig. 10 (b) that the crossover temperature decreases as U increases. Particularly, the second screening stage is more sensitive to U than the first stage which occurs at higher temperature. We can also see that the crossover temperature of the first stage and that of the second one become close for small U . For instance, the two stages take place almost successively for $U/(2\pi t) = 0.2$. Note that the value of the coupling between the TTQD and leads chosen for Fig. 10 is relatively small $\Gamma/t = 0.12$, so that the screening temperature to reach the singlet state becomes very low in the present case, especially for large U . The screening temperature, however, rises as Γ increases. It would make T^* an accessible value in experiments. We will examine the Γ dependence of T^* in Sec. V D.

C. SU(4) Kondo effect at the dip for $N_{\text{tot}} \simeq 3.0$

In this subsection we present the results of the thermodynamic quantities at three-electron filling $N_{\text{tot}} \simeq 3.0$. In Fig. 11, the entropy and spin susceptibility are plotted vs $\log(T/D)$, for $U/(2\pi t) = 1.0$, and $\Gamma/t = 0.12$. The impurity level ϵ_d is chosen in a way such that (a) $\epsilon_d = -0.5897U$ at the zero point of g_s in the middle of the sharp dip seen in Fig. 5, and (b) $\epsilon_d = -0.65U$ ($-0.55U$) at a point on the left (right) of the dip.

We can see in Fig. 11 (a) that at high temperatures $10^{-5} \lesssim T/D \lesssim 10^{-2}$ the entropy is a constant $\mathcal{S} \simeq \log 4$, which is caused by the four-fold degeneracy of the local states in the isolated TTQD cluster mentioned in Sec. II B. Furthermore, the spin susceptibility shows the Curie behavior $\chi \simeq s(s+1)/(3T)$ with $s = 1/2$ at high temperatures. Then, at low temperatures both \mathcal{S} and χT decrease with T . Specifically, the screening of the local four-fold degenerate states is completed in a single stage at $T^*/D \simeq 10^{-7}$. This behavior is observed just at the zero point, at which the two phase shifts are $\delta_e \simeq 5\pi/4$ and $\delta_o \simeq \pi/4$. At the zero point the low-energy excitations from the singlet ground state asymptotically have the channel symmetry in addition to the global SU(2) symmetry of the spin, as shown in Sec. III. Therefore, the low-temperature behavior of these thermodynamic quantities must reflect the low-energy SU(4) symmetry of the fixed-point Hamiltonian. We refer to this zero point of the series conductance at $N_{\text{tot}} \simeq 3.0$ as the SU(4) symmetric point in the following. It should be noted that T^* is enhanced at this point due to the channel degeneracy.

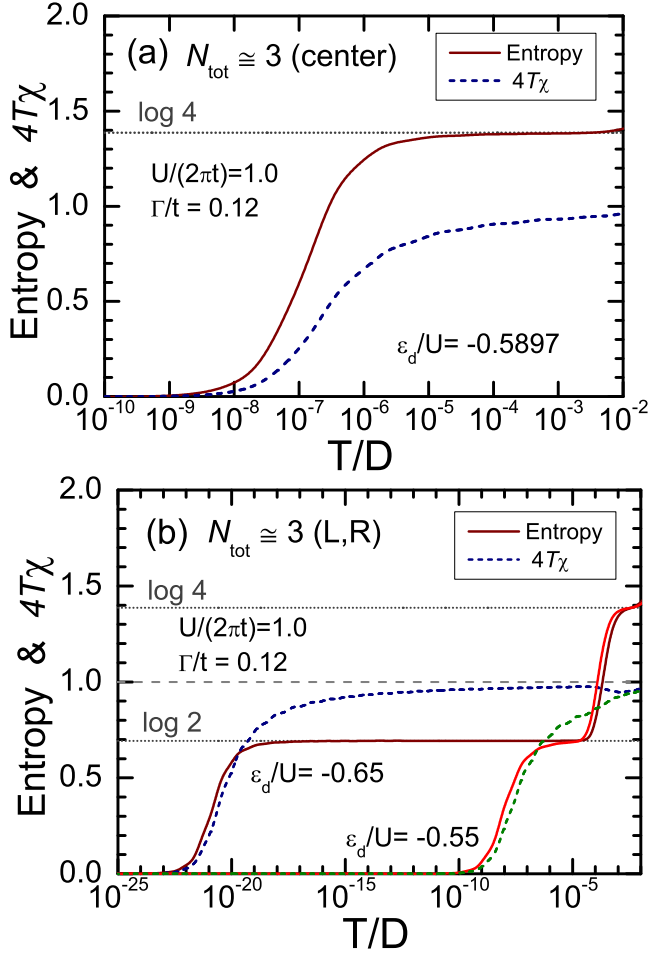


FIG. 11: (Color online) Entropy \mathcal{S} and spin susceptibility $4T\chi$ in the step for $N_{\text{tot}} \simeq 3.0$ are plotted vs $\log(T/D)$ for $t' = t$, $\epsilon_{\text{apex}} = \epsilon_d$ and $\Gamma/t = 0.12$. Impurity level is chosen to be (a) just at the series conductance dip $\epsilon_d = -0.5897U$, (b) on the left $\epsilon_d = -0.65U$ and the right $\epsilon_d = -0.55U$ sides of the dip.

For the values of ϵ_d away from the dip, the entropy shows the two-stage behavior. We can see in Fig. 11 (b) that the entropy still shows the value of $\mathcal{S} \simeq \log 4$ at high temperatures even in the case away from the dip. At intermediate temperatures, however, it takes another plateau with $\mathcal{S} \simeq \log 2$, and the spin susceptibility shows the Curie behavior with the coefficient of $s = 1/2$. Therefore, the orbital part of the degrees of freedom is frozen at intermediate temperatures, and the spin degrees of freedom still remains free. Furthermore, away from dip the low-lying energy excited states no longer have the channel symmetry. The full screening of the remaining spin $1/2$ is completed at $T^*/D \simeq 10^{-21}$ for $\epsilon_d = -0.65U$, and $T^*/D \simeq 10^{-8}$ for $\epsilon_d = -0.55U$. These temperatures are lower than the screening temperature at the SU(4) symmetric point, but still much higher than T^* for the $S = 1$ Kondo effect at $N_{\text{tot}} = 4$, for the same parameter values of U , t , and Γ .

Furthermore, the screening temperature on the right-

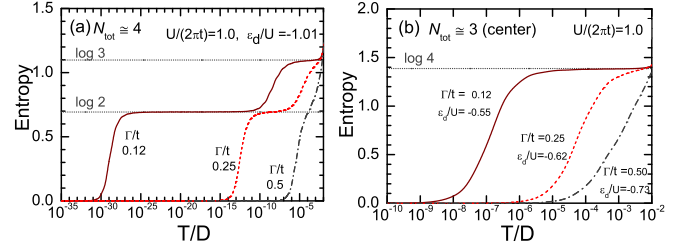


FIG. 12: (Color online) Entropy vs $\log(T/D)$ for several values of Γ ; $U/(2\pi t) = 1.0$ is fixed. Impurity level is chosen to be (a) $\epsilon_d/U = -1.01$ which corresponds to $N_{\text{tot}} \simeq 4.0$, and (b) at the dip in the middle of the step for $N_{\text{tot}} \simeq 3.0$ ($\epsilon_d/U = -0.55, -0.62$, and -0.73 for $\Gamma/t = 0.12, 0.25$, and 0.5 , respectively).

hand side of the SU(4) symmetric point is higher than that on the left-hand side. The difference reflects the charge redistribution, taking place at the conductance dip as discussed in Sec. IV A. As we saw in Fig. 7, the distribution is almost homogenous on the right side; $\langle n_{a,0} \rangle \simeq \langle n_{a,1} \rangle \simeq \langle n_{b,1} \rangle \simeq 1.0$. In contrast, it becomes inhomogeneous on the left side; $\langle n_{a,0} \rangle \simeq 1.0$, $\langle n_{a,1} \rangle \simeq 1.5$ and $\langle n_{b,1} \rangle \simeq 0.5$. In the second screening stage the partial moment in the a_0 orbital, which is singly occupied on average, has to be screened by the electrons coming over the a_1 orbital. Therefore, T^* must be affected by the filling of the a_1 orbital. Specifically, the charge and spin fluctuations at the a_1 orbital, which is necessary for the second stage screening, tends to be frozen as $\langle n_{a,1} \rangle$ approaches to 2.0. The situation is similar to that in the $S = 1$ Kondo case, mentioned in Sec. V B. We will discuss this point further in the next subsection.

The conductances which we discussed in Sec. IV are the results obtained at zero temperature. If the temperature is raised, the series conductance at the SU(4) symmetric point will increase. Simultaneously, the series conductance plateaus on the left- and right-hand sides will decrease. Then, the dip structure will disappear at the temperature of T^* on the left side, because it is the lowest energy scale near the symmetric point. Note that the screening temperature T^* itself varies depending on the parameters Γ , t and U . In order to preserve the typical structure of the dip, however, there are upper and lower bounds for Γ/t and U/t , respectively, as we can see in Figs. 8 and 9.

D. Dependence of the screening temperature on Γ

We consider in this subsection the dependence of the screening temperature T^* on the hybridization Γ and the level position ϵ_d . For comparisons, we have calculated the entropy for several values of the hybridization $\Gamma/t = 0.12, 0.25$ and 0.5 , for a fixed value of the interaction $U/(2\pi t) = 1.0$. The ground state properties for these parameter sets were presented in Figs. 5 and 8.

Figure 12 shows the results obtained at (a) the paral-

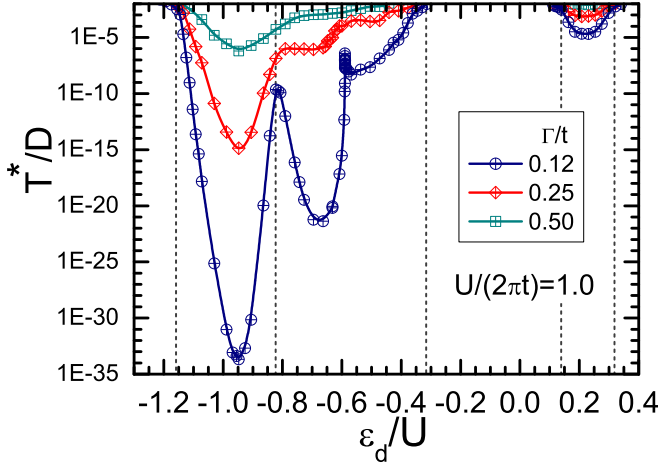


FIG. 13: (Color online) The crossover energy scale T^* as a function of ϵ_d for several values of $\Gamma/t = 0.12, 0.25$, and 0.5 ; $U/(2\pi t) = 1.0$ is fixed. T^* is defined as the temperature in the middle of the low-energy crossover observed in the entropy. The vertical dashed lines correspond to ϵ_d , at which N_{tot} in the limit of $\Gamma = 0$ varies discontinuously.

lel conductance plateau for $N_{\text{tot}} \simeq 4.0$ ($\epsilon_d/U = -1.01$), and (b) the zero point of the series conductance for $N_{\text{tot}} \simeq 3.0$. Therefore, we can see in (a) the Γ dependence of the two-stage screening of the $S = 1$ moment of the Nagaoka state, and in (b) the single-stage SU(4) Kondo behavior. In both of these two cases, the entropy for the intermediate coupling $\Gamma/t = 0.25$ retains the structures which we observed in the weak coupling case $\Gamma/t = 0.12$. For large hybridization $\Gamma/t = 0.5$, however, the charge transfer between the leads and the TTQD brings the system into a mixed-valence regime, and the typical structures are smeared. Furthermore, we can see in (a) and (b) that the crossover temperature T^* is sensitive to the value of the hybridization, and it increases rapidly with the coupling Γ .

We have calculated the entropy also for different fillings, and determined the screening temperature T^* from the mid-point of a low-energy crossover to a singlet ground state. The energy scale T^* defined in this way can be regarded as a Kondo temperature in the case that the system has a well defined local moment at high energies, which is the case of $N_{\text{tot}} \simeq 1.0, 3.0$, and 4.0 . The results of T^* are plotted as a function of ϵ_d in Fig. 13. We see that at the single-electron filling for $0.1U \lesssim \epsilon_d \lesssim 0.3U$ the screening temperature is larger than that of the other regions of the filling. This is because at this filling the single electron enters mainly the a_1 orbital which is connected directly to one of the leads, as illustrated in Fig. 3.

In the region of the three-electron filling $N_{\text{tot}} \simeq 3.0$, the screening temperature is enhanced at the SU(4) symmetric point, $\epsilon_d \simeq -0.59U$, where the series conductance has a dip. We see in Fig. 13 that T^* in the weak hybridization case $\Gamma/t = 0.12$ has a local minimum at $\epsilon_d \simeq -0.65U$ on the left side of the symmetric point, and T^* becomes very

low near the minimum. This is because the fraction of the local spin in the a_0 orbital must be screened indirectly by the conduction electrons coming through the a_1 orbital which is filled already up to $\langle n_{a,1} \rangle \simeq 1.5$. As we see in Fig. 7, there is a significant difference between the charge distribution on the left and right sides of the symmetric point. On the right side, at $-0.58 \lesssim \epsilon_d/U \lesssim -0.4$, the local moment is mainly in the odd-parity b_1 orbital which has a direct tunneling matrix element to one of the leads, as discussed in Sec. IV A. For this reason, the screening temperature on the right side of the dip becomes larger than that on the left side.

We see also in Fig. 13 that the screening temperature is enhanced significantly at $\epsilon_d \simeq -0.82U$ for $\Gamma/t = 0.12$. This seems to be caused by the charge fluctuations between the two different fillings of $N_{\text{tot}} = 3$ and $N_{\text{tot}} = 4$. We note that near this point there is another zero point of the series conductance at $\epsilon_d/U \simeq -0.88$, as we see in Fig. 6. At four-electron filling, T^* becomes small again particularly at $\epsilon_d \simeq -0.95U$. This is because in the second screening stage of the $S = 1$ moment the partial moment in the a_0 site needs to be screened by the electrons from the leads which have no direct hopping matrix elements to the apex site, as mentioned in Sec. V B. We see also that the screening temperature depends sensitively on Γ , as well as on U . Therefore, in order to observe the two-stage behavior experimentally, Γ should be tuned to a large value, but still has to be $\Gamma \lesssim \max(U/3, t)$ in order to retain the typical structures. This criterion is determined by the energy scale $\Delta E^{(4)} \simeq \max(U/3, t)$, defined in Eq. (8).

VI. DEFORMATIONS OF TRIANGLE

So far, we have assumed the full C_{3v} symmetry for the TTQD. Although it has already been broken partly by the connection to the two leads, the perturbations which break the triangular symmetry should be examined further, since real TTQD systems must be deformed from the regular structure to a certain extent. We consider in this section how an asymmetry caused by the inhomogeneity in the level positions and the inter-dot hopping matrix elements affect the ground-state properties.

In the presence of a deformation which is described by ϵ_{apex} and t' , the one-particle energies of the isolated TTQD vary from those for the regular triangle given in Eq. (6) to the following forms

$$E_{e,\pm}^{(1)} = \frac{\epsilon_{\text{apex}} + \epsilon_d - t'}{2} \pm \sqrt{\left(\frac{\epsilon_{\text{apex}} - \epsilon_d + t'}{2}\right)^2 + 2t^2}, \quad (26)$$

$$E_o^{(1)} = \epsilon_d + t'. \quad (27)$$

Here, $E_{e,\pm}^{(1)}$ and $E_o^{(1)}$ are the eigenvalues for the states with even and odd parities, respectively. Note that the system still has the inversion symmetry in the present

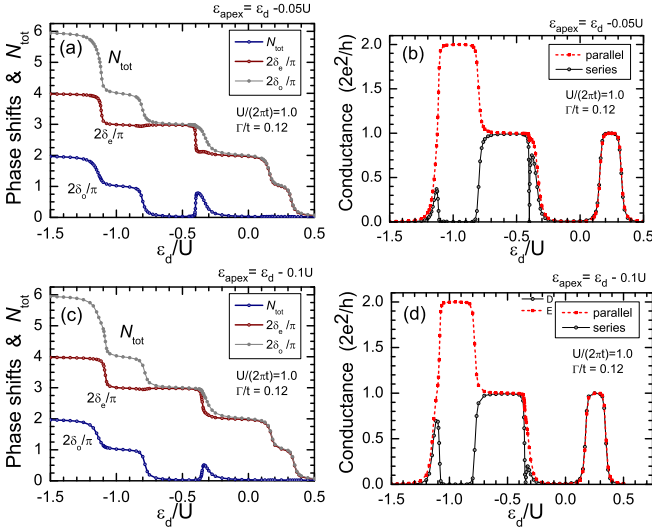


FIG. 14: (Color online) Phase shifts and conductances are plotted vs ϵ_d , keeping the difference between ϵ_{apex} and ϵ_d unchanged; (upper panels) $\epsilon_{\text{apex}} - \epsilon_d = -0.05U$ and (lower panels) $\epsilon_{\text{apex}} - \epsilon_d = -0.1U$, with $U/(2\pi t) = 1.0$, $\Gamma/t = 0.12$ and $t' = t$.

case. Among these three one-particle states, $E_{e,-}^{(1)}$ becomes the lowest energy for small perturbations. The other two excited states become degenerate, $E_{e,+}^{(1)} = E_o^{(1)}$, in the regular triangle case with $t' = t$ and $\epsilon_{\text{apex}} = \epsilon_d$. The deformations lift this degeneracy, and the first order correction with respect to $\delta\epsilon \equiv \epsilon_{\text{apex}} - \epsilon_d$ and $\delta t \equiv t' - t$ is given by

$$E_{e,+}^{(1)} - E_o^{(1)} \simeq \frac{2}{3}\delta\epsilon - \frac{4}{3}\delta t. \quad (28)$$

Thus, the energy of the even state $E_{e,+}^{(1)}$ becomes higher (lower) than that of the odd one $E_o^{(1)}$ for $\delta\epsilon - 2\delta t > 0$ (< 0). It reflects the fact that the apex site with ϵ_{apex} belongs to the even part of the basis. Furthermore, t' shifts the onsite potential of the b_1 orbital upwards, and that of the a_1 downwards. In the following, we examine effects of $\delta\epsilon$ and δt separately, in a wide range of the electron filling N_{tot} .

In Figs. 14 and 15, the NRG results of the conductances and phase shifts are plotted as functions of ϵ_d for several fixed values of $\delta\epsilon$, with $\delta t = 0$. The values of ϵ_{apex} are chosen such that $\delta\epsilon/U = -0.05, -0.1$ for Fig. 14, and $\delta\epsilon/U = 0.05, 0.1$ for Fig. 15. The other parameters U and Γ are chosen to be the same as those for Fig. 5.

We see in (b) and (d) of both Figs. 14 and 15 that the series conductance dip emerges in the Kondo plateau at three-electron filling $N_{\text{tot}} \simeq 3.0$ even in the presence of the small deformations. Particularly, the typical feature of the sharp dip clearly remains. The position of the dip, however, shifts sensitively to $\delta\epsilon$, and it moves towards the right (left) for $\delta\epsilon < 0$ ($\delta\epsilon > 0$). This reflects the behavior of the phase shifts at $-0.8U \lesssim \epsilon_d \lesssim -0.3U$ in (a) and (c)

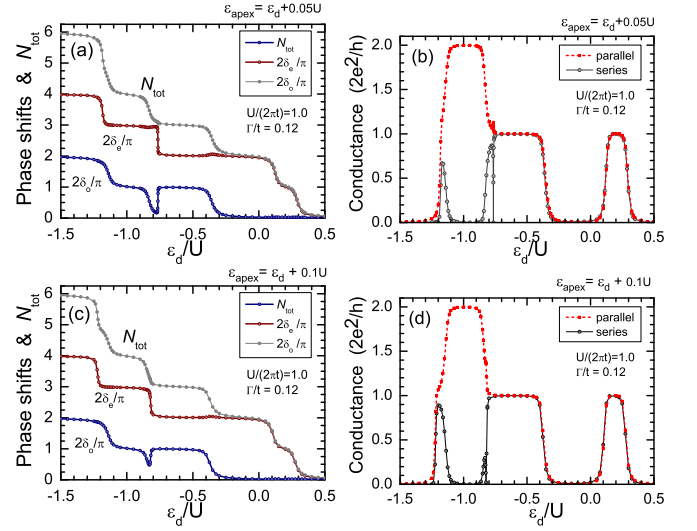


FIG. 15: (Color online) Phase shifts and conductances are plotted vs ϵ_d , keeping the difference between ϵ_{apex} and ϵ_d unchanged; (upper panels) $\epsilon_{\text{apex}} - \epsilon_d = 0.05U$ and (lower panels) $\epsilon_{\text{apex}} - \epsilon_d = 0.1U$, with $U/(2\pi t) = 1.0$, $\Gamma/t = 0.12$ and $t' = t$.

of these figures. Particularly, the odd phase shift δ_o shows a clear contrast between the positive and negative $\delta\epsilon$. Correspondingly the kink, which is seen in the even phase shift as a step between the values of $2\delta_e/\pi = 2.0$ and 3.0 , moves as $\delta\epsilon$ varies. When the gate voltage ϵ_d decreases from a value at two-electron filling, the third electron enters mainly the b_1 orbital until ϵ_d reaches the SU(4) symmetric point, at which point the charge distribution changes significantly as seen in Fig. 7. The redistribution of the charge is protracted for $\delta\epsilon > 0$, because the odd orbital becomes energetically favorable $E_{e,+}^{(1)} > E_o^{(1)}$. In the opposite case, for $E_{e,+}^{(1)} < E_o^{(1)}$, the redistribution takes place earlier than the regular triangle case. As the magnitude $|\delta\epsilon|$ of the deformations increases further, the conductance dip moves away from the Kondo plateau and disappears. The range of $|\delta\epsilon|$, in which the dip can be seen, will increase with the width of the Kondo plateau.

Another notable change caused by the deformations due to $\delta\epsilon$ is the structure at five electron filling $N_{\text{tot}} \simeq 5.0$. We see in (b) and (d) of both Figs. 14 and 15 that a peak of the series conductance evolves at $-1.2U \lesssim \epsilon_d \lesssim -1.1U$, as $|\delta\epsilon|$ increases. Simultaneously, in this region, the parallel conductance has a gentle shoulder. Furthermore, we can see also in (c) of in these figures that a weak step for the five-electron occupancy emerges for N_{tot} in the case of $\delta\epsilon = \pm 0.1U$.

In the other regions of the filling, namely at $N_{\text{tot}} \simeq 4.0$ and $N_{\text{tot}} \lesssim 2.0$, the conductances and phase shifts are less sensitive to the small perturbations due to $\delta\epsilon$. Specifically, the $S = 1$ Kondo behavior is robust, although the region of ϵ_d for the four-electron filling becomes slightly narrow. As mentioned in Sec. IIB, the Nagaoka state is the ground state of the TTQD for $N_{\text{tot}} = 4$ in the

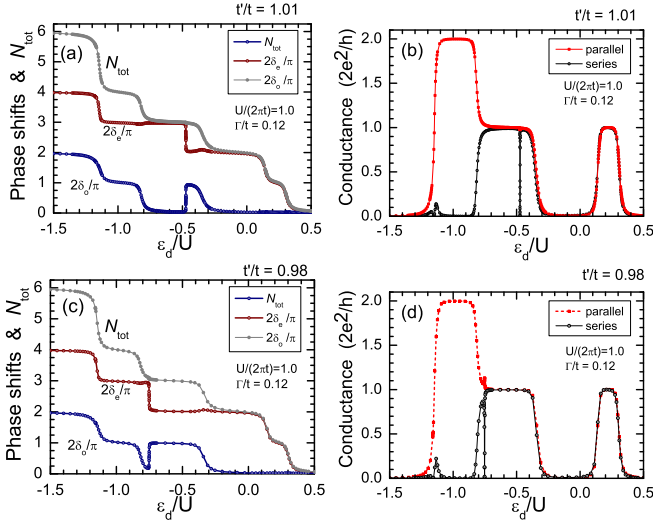


FIG. 16: (Color online) Phase shifts and conductances as functions of ϵ_d , for (upper panels) $t' = 1.01t$ and (lower panels) $t' = 0.98t$, with $U/(2\pi t) = 1.0$, $\Gamma/t = 0.12$ and $\epsilon_{\text{apex}} = \epsilon_d$.

limit of $\Gamma = 0$. We have calculated the cluster eigenstates in the presence of the deformations, and found that the Nagaoka state remains as the ground state near $\epsilon_d/U \simeq -1.0$ in a wide range of the deformation $-0.41U < \delta\epsilon < 0.87U$ for $U/(2\pi t) = 1.0$. This is determined mainly by the finite-size energy separation $\Delta E^{(4)} \equiv E_{S=0}^{(4)} - E_{S=1}^{(4)}$ between the Nagaoka and the lowest singlet states, mentioned in Sec. II B. This energy scale of the TTQD makes the $S = 1$ Kondo behavior rigid also against the deformations.

We have examined also the effects of small deformations caused by the hopping matrix elements $\delta t = t' - t$, choosing the level positions to be uniform $\delta\epsilon = 0$. In Fig. 16, the conductances and phase shifts are plotted as functions of ϵ_d for $t' = 1.01t$ (upper panels), and for $t' = 0.98t$ (lower panels). Besides huge similarities to the above results for the case of $\delta\epsilon$, one notable difference is that no pronounced structures evolve at $N_{\text{tot}} = 5.0$ for small δt . In the cluster limit $\Gamma = 0$, the five-electron charge state can become the ground state for finite δt , but in a very narrow region near $\epsilon_d \simeq -1.16U$, the width of which $\Delta\epsilon_d$ is calculated to be $\Delta\epsilon_d \simeq 0.004U$ for $t'/t = 0.98$, and $\Delta\epsilon_d \simeq 0.002U$ for $t'/t = 1.01$. This energy scale is much smaller than the hybridization strength $\Gamma = 0.019U$, and thus quantitatively the five-electron structure was not seen in the present situation.

In the other regions of the filling, however, the results obtained for $\delta t > 0$ and $\delta t < 0$ resemble those for $\delta\epsilon < 0$ and $\delta\epsilon > 0$, respectively. Particularly, the structures of the series conductance dip and the phase shifts at $N_{\text{tot}} \simeq 3.0$ are similar qualitatively to those seen in the upper panels of Figs. 14 and 15. These features are determined essentially by the way that the orbital degeneracy between the even and odd orbitals is lifted, namely $E_{e,+}^{(1)} < E_o^{(1)}$ or $E_{e,+}^{(1)} > E_o^{(1)}$. The $SU(4)$ Kondo effect

is sensitive to relatively small deformations, because it relies on the orbital degeneracy at three-electron filling. Nevertheless, the sharp structure of the dip does not collapse immediately under an infinitesimal perturbation, and thus a perfect C_{3v} symmetry is not necessary to observe the $SU(4)$ Kondo behavior in the TTQD.

The $S = 1$ Kondo behavior at the four-electron filling is not sensitive to δt , as that in the case of small $\delta\epsilon$. We have confirmed also that the Nagaoka state remains as a ground state of the isolated TTQD cluster near $\epsilon_d/U \simeq -1.0$ also in a wide range of the off-diagonal inhomogeneity $0.30 < t'/t < 2.87$ for $U/(2\pi t) = 1.0$. The $S = 1$ Kondo behavior is robust also against the deformations by δt , and it is mainly due to the finite-size energy separation of $\Delta E^{(4)}$.

VII. SUMMARY

We have discussed first of all in Sec. III that the fixed-point Hamiltonian which describes the low-lying energy excitation from a local Fermi-liquid ground state has an $SU(4)$ symmetry, consisting of the channel and spin degrees of freedom, at zero points of the two-terminal conductance, or equivalently at the points where the two phase shifts satisfy the condition $\delta_e - \delta_o = n\pi$ for $n = 0, \pm 1, \pm 2, \dots$. This symmetry property holds at low energies quite generally for the systems which can be described by the Hamiltonian \mathcal{H} given in Eq. (1), for any numbers of quantized levels N_D , in the case that the system has time-reversal and inversion symmetries. Specifically, the Hamiltonian \mathcal{H} does not necessarily have an $SU(4)$ symmetry on the global energy scale.

In the main part of the paper we have discussed the Kondo effects taking place in the triangular triple quantum dot connected to two non-interacting leads, as illustrated in Fig. 1. We have deduced from the difference between the two phase shifts shown in Fig. 6 that the two-terminal conductance of this system can have three zero points as the level position ϵ_d varies. The low-energy properties at these zero points can be characterized by the $SU(4)$ symmetric local Fermi-liquid theory. Particularly, the zero point at three-electron filling appears as a sharp dip in the middle of the conductance plateau seen in Fig. 5. At this zero point the phase shifts satisfy the conditions $\delta_e - \delta_o = \pi$ and $\delta_e + \delta_o \simeq 3\pi/2$, which means that $\delta_e \simeq 5\pi/4$ and $\delta_o \simeq \pi/4$. Furthermore, at this filling, the system has an $SU(4)$ symmetry also at high energies, which is caused by the four-fold degeneracy in the local states of an isolated triangular cluster. These symmetry properties at two opposite limits, at low and high energies, cause a single-stage screening observed in temperature dependence of the entropy shown in Fig. 11.

For the values of ϵ_d away from the dip, the system no longer has the low-energy $SU(4)$ symmetry, and the low-lying energy excited states have only the $SU(2)$ symmetry of the spin. We have confirmed also that the charge distribution in the even and odd orbitals, the geometrical

feature of which is illustrated in Fig. 3, changes significantly at the dip as shown in Fig. 7. The inhomogeneous charge distribution in the even-odd basis also causes the two-stage Kondo behavior of the $S = 1$ local moment which emerges at four-electron fillings due to Nagaoka ferromagnetic mechanism. The partial moment which is distributed away from the two leads makes the Kondo temperature for the second stage very small. Nevertheless, the Kondo temperature can be raised by increasing the coupling Γ between the TTQD and leads. Therefore, in order to observe the second screening stage, Γ should be large. At the same time, however, Γ has to be smaller than $\Delta E^{(4)} \simeq \max(U/3, t)$ so that the hybridization effects should not smear the typical structures of the $S = 1$ Kondo behavior.

We have studied also the effects of the deformations, which break the full triangular symmetry C_{3v} and lift the orbital degeneracy in the one-particle excited states. Specifically, the deformations which are caused by inhomogeneity in the onsite potentials $\delta\epsilon \equiv \epsilon_{\text{apex}} - \epsilon_d$ and the inter-dot couplings $\delta t \equiv t' - t$ have been examined. We found that the series conductance dip does still exist stably at three-electron filling, even in the presence of infinitesimal deformations. The position of the dip, however, shifts sensitively from the middle of the Kondo plateau for $N_{\text{tot}} \simeq 3.0$. In the other region of the fillings, small deformations do not affect the Kondo behavior significantly, and just cause some gradual and quantitative changes. These results support our belief that the various Kondo effects in the TTQD could be observed in future.

Acknowledgments

We would like to thank S. Amaha, J. Bauer, V. Meden, Yoichi Tanaka and Y. Utsumi for valuable discussions. This work is supported by JSPS Grant-in-Aid for Scientific Research (C). One of us (ACH) acknowledges the support of a grant from the EPSRC (G032181/1). Numerical computation was partly carried out in Yukawa Institute Computer Facility.

APPENDIX A: NAGAOKA STATE IN A TRIANGLE

The eigenvector of the Nagaoka state $|\Phi_{S=1}^{(4)}\rangle$ for the isolated triangle with $t' = t$ and $\epsilon_{\text{apex}} = \epsilon_d$ can be constructed simply, by filling first the one-particle state of $k = 0$ defined in (6) by two electrons, and then filling each of the two excited states with $k = +2\pi/3$ and $k = -2\pi/3$ by a single up-spin electron. This state can be expressed, using the even and orbitals described in Eq. (16) and Fig. 3, in the form

$$|\Phi_{S=1}^{(4)}\rangle = \alpha_0 |\text{I}\rangle + \alpha_1 |\text{II}\rangle, \quad (\text{A1})$$

$$|\text{I}\rangle = b_{1\uparrow}^\dagger a_{0\uparrow}^\dagger a_{1\uparrow}^\dagger a_{0\downarrow}^\dagger |0\rangle, \quad |\text{II}\rangle = b_{1\uparrow}^\dagger a_{0\uparrow}^\dagger a_{1\uparrow}^\dagger a_{1\downarrow}^\dagger |0\rangle. \quad (\text{A2})$$

Here, $\alpha_0 = \sqrt{1/3}$, $\alpha_1 = \sqrt{2/3}$, $|0\rangle$ is a vacuum, and the eigenvalue is give by $E_{S=1}^{(4)} = -2t + U + 4\epsilon_d$. This state has a finite total-spin z component of $S_z = +1$, and breaks the spin rotational symmetry. In this state, the partial moments for even orbitals are given by

$$\begin{aligned} m_{a,i} &\equiv \langle \Phi_{S=1}^{(4)} | \frac{1}{2} (a_{i\uparrow}^\dagger a_{i\uparrow} - a_{i\downarrow}^\dagger a_{i\downarrow}) | \Phi_{S=1}^{(4)} \rangle \\ &= \frac{1}{2} (1 - |\alpha_i|^2). \end{aligned} \quad (\text{A3})$$

Thus, $m_{a,0} = 1/3$, $m_{a,1} = 1/6$, and the partial moment in the odd orbital b_1 is given by $m_{b,1} = 1/2$. Furthermore, the occupation number of each orbital takes the value $\langle n_{a,0} \rangle = 4/3$, $\langle n_{a,1} \rangle = 5/3$, and $\langle n_{b,1} \rangle = 1$.

In the subspace with $N_{\text{tot}} = 4$ and $S = 1$, the matrix elements of the interaction Hamiltonian has a diagonal form

$$\langle \nu | \mathcal{H}_{\text{dot}}^U | \nu' \rangle = U \delta_{\nu, \nu'}, \quad (\text{A4})$$

for $\nu, \nu' = \text{I, II}$. This can be verified directly using Eq. (19). For this reason, the wavefunction is determined by the noninteracting Hamiltonian, which can be rewritten generally in the following form (see also Fig. 3)

$$\begin{aligned} \mathcal{H}_{\text{dot}}^0 &= \epsilon_{\text{apex}} n_{a,0} + (\epsilon_d - t') n_{a,1} + (\epsilon_d + t') n_{b,1} \\ &\quad - \sqrt{2} t \sum_{\sigma} (a_{0\sigma}^\dagger a_{1\sigma} + a_{1\sigma}^\dagger a_{0\sigma}). \end{aligned} \quad (\text{A5})$$

Therefore, the coefficients α_0 and α_1 defined in Eq. (A2) depend crucially on the potential difference between the a_0 and a_1 orbitals, which correspond to the first and second terms in the right-hand side of Eq. (A5). This potential profile in the even-odd basis play an important role on the two-stage Kondo effects, which take place in the case that the two leads are connected to the a_1 and b_1 orbitals in the way that is shown in Fig. 3.

APPENDIX B: MANY-BODY PHASE SHIFTS

The phase shifts for interacting electrons can be defined, using the Green's function

$$G_{ij}(i\omega_n) = - \int_0^\beta d\tau \langle T_\tau d_{i\sigma}(\tau) d_{j\sigma}^\dagger(0) \rangle e^{i\omega_n \tau}, \quad (\text{B1})$$

where $\beta = 1/T$, $d_{j\sigma}(\tau) = e^{\tau \mathcal{H}} d_{j\sigma} e^{-\tau \mathcal{H}}$, and $\langle \mathcal{O} \rangle = \text{Tr} [e^{-\beta \mathcal{H}} \mathcal{O}] / \text{Tr} e^{-\beta \mathcal{H}}$. The retarded and advanced Green's functions correspond to the analytic continuations $G_{ij}^\pm(\omega) = G_{ij}(\omega \pm i0^+)$. The interaction $\mathcal{H}_{\text{dot}}^U$ between electrons in the dots at $1 \leq i \leq N_D$ ($N_D = 3$ for the triple dot) causes the self-energy correction $\Sigma_{ij}(z)$, and the Dyson equation is given by

$$G_{ij}(z) = G_{ij}^0(z) + \sum_{i'=1}^{N_D} \sum_{j'=1}^{N_D} G_{ii'}^0(z) \Sigma_{i'j'}(z) G_{j'j}(z). \quad (\text{B2})$$

Here, $G_{ij}^0(z)$ is the non-interacting Green's function corresponding to $\mathcal{H}_0 \equiv \mathcal{H}_{\text{dot}}^0 + \mathcal{H}_{\text{mix}} + \mathcal{H}_{\text{lead}}$.

At zero temperature $T = 0$, the series g_s and parallel g_p conductances can be expressed in terms of the Green's function at the Fermi level $\omega = 0$, in the case the system has a time-reversal symmetry^{19,23}

$$g_s = \frac{2e^2}{h} 4\Gamma_R \Gamma_L |G_{ND1}^+(0)|^2, \quad (\text{B3})$$

$$g_p = \frac{2e^2}{h} \left[\Gamma_L^2 |G_{11}^+(0)|^2 + \Gamma_R^2 |G_{NDND}^+(0)|^2 + 2\Gamma_L \Gamma_R |G_{ND1}^+(0)|^2 \right] \quad (\text{B4})$$

$$= \frac{2e^2}{h} \left[-\Gamma_L \text{Im} G_{11}^+(0) - \Gamma_R \text{Im} G_{NDND}^+(0) \right]. \quad (\text{B5})$$

Note that the contributions of the vertex correction do not appear here due to the property that the imaginary part of the self-energy vanishes $\text{Im} \Sigma_{ij}^\pm(0) = 0$ at $T = 0$ and $\omega = 0$.⁵⁵ Therefore the value of $G_{ij}^+(0)$ appearing in the above equations can be reproduced correctly by a free quasi-particle Hamiltonian $\mathcal{H}_{\text{eff}} \equiv \tilde{\mathcal{H}}_{\text{dot}} + \mathcal{H}_{\text{mix}} + \mathcal{H}_{\text{lead}}$,

$$\tilde{\mathcal{H}}_{\text{dot}} \equiv - \sum_{i,j=1}^{N_D} \sum_{\sigma} \tilde{t}_{ij} d_{i\sigma}^\dagger d_{j\sigma}. \quad (\text{B6})$$

Here, $-\tilde{t}_{ij} = -t_{ij} + \epsilon_{d,i} \delta_{ij} + \text{Re} \Sigma_{ij}^+(0)$ can be regarded as the hopping matrix element for free quasi-particles.^{19,55}

Furthermore, in the case the system has also the inversion symmetry $\Gamma_L = \Gamma_R$ ($\equiv \Gamma$), the Green's functions take the form

$$G_{11}^+(0) = G_{NDND}^+(0) = \frac{1}{2\Gamma} \left[\frac{1}{\kappa_e + i} + \frac{1}{\kappa_o + i} \right], \quad (\text{B7})$$

$$G_{ND1}^+(0) = \frac{1}{2\Gamma} \left[\frac{1}{\kappa_e + i} - \frac{1}{\kappa_o + i} \right]. \quad (\text{B8})$$

Here, $\kappa_e = -\cot \delta_e$ and $\kappa_o = -\cot \delta_o$ include all the many-body corrections through the real part of the self-energy $\text{Re} \Sigma_{ij}^+(0)$.²³ Equations (10)–(12) follow from Eqs.

(B3)–(B8). One can state immediately from Eq. (B8) that the series conductance g_s becomes zero in the case $\kappa_e = \kappa_o$, or equally for $\delta_e - \delta_o = n\pi$ for $n = 0, \pm 1, \pm 2, \dots$

APPENDIX C: NRG APPROACH

In the NRG approach the non-interacting leads are transformed into the chains carrying out the logarithmic discretization with the parameter Λ , and a sequence of the Hamiltonian H_N in the following form is introduced,^{52,53}

$$H_N = \Lambda^{(N-1)/2} \left(\mathcal{H}_{\text{dot}}^0 + \mathcal{H}_{\text{dot}}^U + H_{\text{mix}} + H_{\text{lead}}^{(N)} \right), \quad (\text{C1})$$

$$H_{\text{mix}} = \bar{v} \sum_{\sigma} \left(f_{0,L\sigma}^\dagger d_{1,\sigma} + d_{1,\sigma}^\dagger f_{0,L\sigma} \right) + \bar{v} \sum_{\sigma} \left(f_{0,R\sigma}^\dagger d_{N_C,\sigma} + d_{N_C,\sigma}^\dagger f_{0,R\sigma} \right), \quad (\text{C2})$$

$$H_{\text{lead}}^{(N)} = D \frac{1+1/\Lambda}{2} \sum_{\nu=L,R} \sum_{\sigma} \sum_{n=0}^{N-1} \xi_n \Lambda^{-n/2} \times \left(f_{n+1,\nu\sigma}^\dagger f_{n,\nu\sigma} + f_{n,\nu\sigma}^\dagger f_{n+1,\nu\sigma} \right). \quad (\text{C3})$$

Here, D is the half-width of the conduction band, and the other parameters are given by^{52,53}

$$\bar{v} = \sqrt{\frac{2D\Gamma A_\Lambda}{\pi}}, \quad A_\Lambda = \frac{1}{2} \frac{1+1/\Lambda}{1-1/\Lambda} \log \Lambda, \quad (\text{C4})$$

$$\xi_n = \frac{1 - 1/\Lambda^{n+1}}{\sqrt{1 - 1/\Lambda^{2n+1}} \sqrt{1 - 1/\Lambda^{2n+3}}}. \quad (\text{C5})$$

The factor A_Λ represents a correction to the discrete model for comparison with results in the continuum limit $\Lambda \rightarrow 1$.^{52,56} We have carried out the iterative diagonalization of H_N using the even-odd basis defined in Sec. II D.

¹ L. I. Glazman and M. E. Raikh, JETP Lett. **47**, 452 (1988).

² T. K. Ng and P. A. Lee, Phys. Rev. Lett. **61**, 1768 (1988).

³ D. Goldharber-Gordon, H. Shtrikman, D. Mahalu, D. Abusch-Magder, U. Meirav, and M. A. Kastner, Nature **391**, 156 (1998).

⁴ S. M. Cronenwett, T. H. Oosterkamp, and L. P. Kouwenhoven, Science **281**, 540 (1998).

⁵ H. Akera, Phys. Rev. B **47**, 6835 (1993).

⁶ W. Izumida, O. Sakai, and Y. Shimizu, J. Phys. Soc. Jpn. **66**, 717 (1997).

⁷ W. Hofstetter, J. König, and H. Schoeller, Phys. Rev. Lett. **87**, 156803 (2001).

⁸ K. Kobayashi, H. Aikawa, S. Katsumoto, and Y. Iye, Phys. Rev. Lett. **88**, 256806 (2002).

⁹ L. I. Glazman and K. A. Matveev, JETP Lett. **49**, 659 (1989).

¹⁰ A. A. Clerk and V. Ambegaokar, Phys. Rev. B **61**, 9109 (2000).

¹¹ A. V. Rozhkov and D. P. Arovas, Phys. Rev. Lett. **82**, 2788 (1999).

¹² M. R. Buitelaar, T. Nussbaumer and C. Schönenberger, Phys. Rev. Lett. **89**, 256801 (2002).

¹³ J. Bauer, A. Oguri, and A. C. Hewson, J. Phys.: Condes. Mat. **19**, 486211 (2007).

¹⁴ C. Karrasch, A. Oguri, and V. Meden, Phys. Rev. B **77**, 024517 (2008).

¹⁵ Yoichi Tanaka, N. Kawakami, and A. Oguri, Phys. Rev. B **78**, 035444 (2008).

- ¹⁶ W. Izumida, O. Sakai, and Y. Shimizu, J. Phys. Soc. Jpn. **67**, 2444 (1998).
- ¹⁷ W. Izumida and O. Sakai, Phys. Rev. B **62**, 10260 (2000).
- ¹⁸ A. Oguri, Phys. Rev. B **59**, 12240 (1999).
- ¹⁹ A. Oguri, Phys. Rev. B **63**, 115305 (2001); **63**, 249901(E) (2001).
- ²⁰ T. Kuzmenko, K. Kikoin and Y. Avishai, Phys. Rev. Lett. **96**, 046601 (2006).
- ²¹ A. Oguri, Y. Nisikawa, Y. Tanaka, and T. Numata, J. Magn. & Magn. Mater. **310**, 1139 (2007).
- ²² A. Oguri and A. C. Hewson, J. Phys. Soc. Jpn. **74**, 988 (2005); **75**, 128001(E) (2006).
- ²³ A. Oguri, Y. Nisikawa and A. C. Hewson, J. Phys. Soc. Jpn. **74**, 2554 (2005).
- ²⁴ Y. Nisikawa and A. Oguri, Phys. Rev. B **73**, 125108 (2006).
- ²⁵ T. Kuzmenko, K. Kikoin and Y. Avishai, Phys. Rev. B **73**, 235310 (2006).
- ²⁶ R. Žitko, J. Bonča, A. Ramšak, and T. Rejec, Phys. Rev. B **73**, 153307 (2006).
- ²⁷ R. Žitko, and J. Bonča, Phys. Rev. Lett. **98**, 047203 (2007).
- ²⁸ M. Eto and Y. V. Nazarov, Phys. Rev. Lett. **85**, 1306 (2000).
- ²⁹ R. Sakano, and N. Kawakami, Phys. Rev. B **72**, 085303 (2005).
- ³⁰ L. De Leo and M. Fabrizio, Phys. Rev. Lett. **94**, 236401 (2005).
- ³¹ T. Kita, R. Sakano, T. Ohashi, and S. Suga, J. Phys. Soc. Jpn. **77**, 094707 (2008).
- ³² T. Hecht, A. Weichselbaum, Y. Oreg, J. von Delft, arXiv:0805.3145.
- ³³ S. Schmaus, V. Koerting, J. Paaske, T. S. Jespersen, J. Nygård, P. Wölfe, arXiv:0809.1969.
- ³⁴ A. Vidan, R. M. Westervelt, M. Stopa, M. Hanson and A. C. Gossard, Appl. Phys. Lett. **85**, 3602 (2004).
- ³⁵ L. Gaudreau, S. A. Studenikin, A. S. Sachrajda, P. Zawadzki, A. Kam, J. Lapointe, M. Korkusinski, and P. Hawrylak, Phys. Rev. Lett. **97**, 036807 (2006).
- ³⁶ S. Amaha, T. Hatano, T. Kubo, Y. Tokura, D. G. Austing, and S. Tarucha, Physica E **40**, 1322 (2008).
- ³⁷ S. Amaha, T. Hatano, S. Teraoka, S. Tarucha, Y. Nakata, T. Miyazaki, T. Oshima, T. Usuki, and N. Yokoyama, Appl. Phys. Lett. **92**, 202109 (2008).
- ³⁸ K. Grove-Rasmussen, H. I. Jørgensen, T. Hayashi, P. E. Lindelof, and T. Fujisawa, Nano Lett. **8**, 1055 (2008).
- ³⁹ T. Jamneala, V. Madhavan, and M. F. Crommie, Phys. Rev. Lett. **87**, 256804 (2001).
- ⁴⁰ K. Ingersent, A. W. W. Ludwig and I. Affleck, Phys. Rev. Lett. **95**, 257204 (2005).
- ⁴¹ B. Lazarovits, P. Simon, G. Zaránd, and L. Szunyogh, Phys. Rev. Lett. **95**, 077202 (2005).
- ⁴² T. Numata, Y. Nisikawa, A. Oguri, and A. C. Hewson, J. Phys.: Conference Series **150**, 022067 (2009).
- ⁴³ R. Žitko and J. Bonča, Phys. Rev. B **77**, 245112 (2008).
- ⁴⁴ A. K. Mitchell, T. Jarrold, and D. E. Logan, arXiv:0902.4816.
- ⁴⁵ E. Vernek, C. A. Büsser, G. B. Martins, E. V. Anda, N. Sandler and S. E. Ulloa, arXiv:0902.2926.
- ⁴⁶ L. Borda, G. Zaránd, W. Hofstetter, B. I. Halperin, and J. von Delft, Phys. Rev. Lett. **90**, 026602 (2003).
- ⁴⁷ M. R. Galpin, D. E. Logan, and H. R. Krishnamurthy, J. Phys.: Condens. Matt. **18**, 6545 (2006).
- ⁴⁸ J. Mravlje, A. Ramšak, and T. Rejec, Phys. Rev. B **73**, 241305(R) (2006).
- ⁴⁹ F. B. Anders, D. E. Logan, M. R. Galpin, and G. Finkelstein, Phys. Rev. Lett. **100**, 086809 (2008).
- ⁵⁰ Y. Nagaoka, Phys. Rev. **147**, 392 (1966).
- ⁵¹ A. Kawabata, J. Phys. Soc. Jpn. **60**, 3222 (1991).
- ⁵² H. R. Krishna-murthy, J. W. Wilkins, and K. G. Wilson, Phys. Rev. B **21**, 1003 (1980).
- ⁵³ H. R. Krishna-murthy, J. W. Wilkins, and K. G. Wilson, Phys. Rev. B **21**, 1044 (1980).
- ⁵⁴ A. C. Hewson, A. Oguri, and D. Meyer, Eur. Phys. J. B **40**, 177 (2004).
- ⁵⁵ A. Oguri, J. Phys. Soc. Jpn. **70**, 2666 (2001).
- ⁵⁶ R. Bulla, T. Costi, T. Pruschke, Rev. Mod. Phys. **80**, 395 (2008).